FERMILAB-THESIS-1990-15

Z^0 Production Cross Section at the Fermilab Tevatron

A thesis presented

by

Edward Thomas Kearns

to

The Department of Physics

in partial fulfillment of the requirements

for the degree of

Doctor of Philosophy

in the subject of

Physics

Harvard University

Cambridge, Massachusetts

June, 1990

Abstract

The cross section times branching ratio for $\bar{p}p \rightarrow Z^0 \rightarrow e^+e^-$ at $\sqrt{s} = 1800$ GeV is measured as 204 ± 13(stat.) $\pm$ 7(sys.) $\pm$ 31(lum.) pb from 4.05 pb^{-1} of CDF data from the Fermilab Tevatron.

Acknowledgements

Like any other CDF result, this measurement relied on the hard work of many CDF and Fermilab physicists and technical staff. In addition to my overall gratitude to all who built the foundation for this work, I'd like to specifically thank a few who have made an outstanding contribution. My friends and coworkers Johnny Ng and Peter Hurst were always available to share meals, diversions and (gratefully) the workload. Keith Ellis provided the programs for the theoretical calculations, complete with prompt and clear answers to all of my questions. Most important of all was Melissa Franklin; her indefatigable support was the key ingredient in bringing this to completion. Melissa and George Brandenburg carefully proofread my thesis and helped turn my tortured drafts into comprehensible prose.

Of course, there was more than this thesis to my graduate student years. Again, there are a multitude of friends who have shared my time and coworkers who have shared my many projects. I could not do justice in listing and thanking them individually. I just hope they recognized my appreciation when it was due.

But I will here thank the five physicists who guided my education: Roy Schwitters, George Brandenburg, Craig Blocker, Marjorie Shapiro and Melissa Franklin. Each contributed uniquely to the spirit of inquiry and critical thought present in our group. They were my source for technical knowledge, scientific intuition, personal advice and emotional support. I have been enriched by being their student, and fortunate to also have them as friends.

Yet one other person stands out above all; she provided balance to my life and respite from the trials of my work. To Heidi, I dedicate my thesis.

Contents

Chapter 1

Introduction

One of the primary objectives of $\bar{p}p$ experiments is to explore the Standard Model [1]. The model uses the intermediate vector bosons $W^{\pm}$ and Z^0 to describe the weak interactions. In 1982, the CERN proton-antiproton collider began operating at a high enough energy to produce these particles in the final state. Soon the W particle was detected by its characteristic signature of a single high energy lepton balanced by large missing transverse energy ($\not{E}_t$) [2, 3]. The Z^0 was found through its decay into two high energy leptons with an invariant mass around 90 GeV [4, 5]. The CERN program continued to explore the nature of these particles [6, 7]. In 1987 it was joined in this effort by the CDF experiment operating at the Fermilab Tevatron.

The topic of this thesis is the production cross section times branching ratio into electrons for the Z^0 boson in $\bar{p}p$ collisions at a center-of-mass energy of 1.8 TeV. The Z^0 is produced by quark-antiquark annihilation and it immediately decays into other fermion-antifermion pairs. The experimental signal for the $Z^0 \rightarrow e^+e^-$ are events with high transverse energy electrons that form a narrow mass resonance at 91 GeV. Figure 1.1 is a CDF event display of a candidate event, showing the electron energy in the calorimeters. The resonance is superimposed on a falling spectrum of dielectron masses from virtual photons γ^* produced by quark-antiquark annihilation.

To obtain the cross-section, we employ the formula:

$$\sigma \cdot \mathrm{B} = \frac{N_Z - N_{\text{background}}}{\epsilon \cdot \mathcal{L}}. \tag{1.1}$$

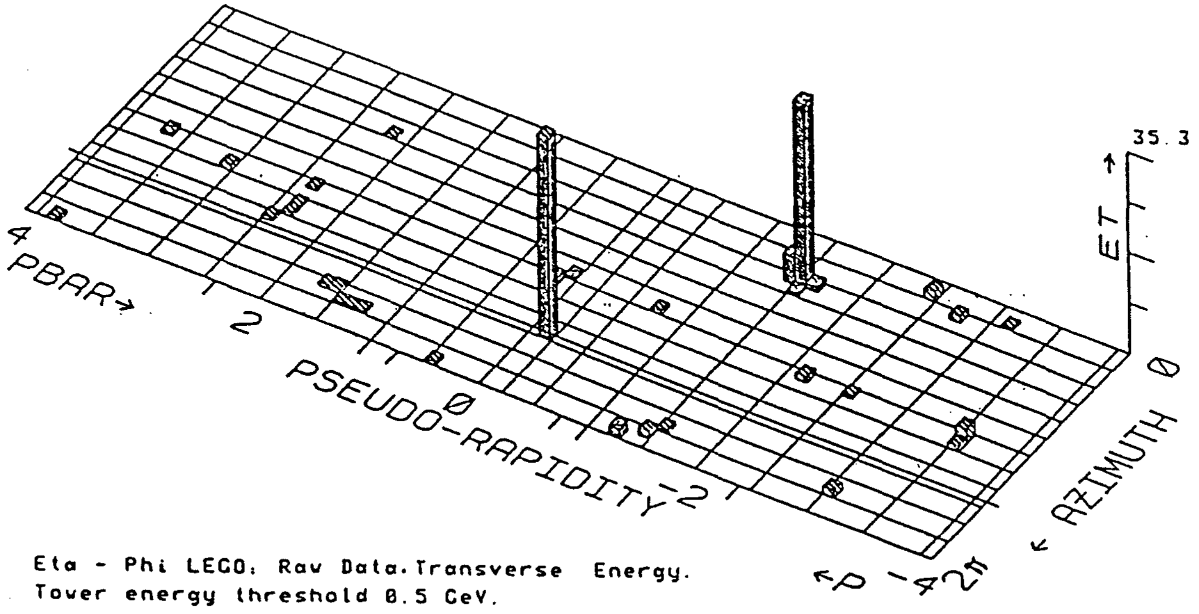

Figure 1.1: A Z^0 event as seen in the CDF calorimeters.

Thus, this measurement relies on identifying N_Z events using kinematic and electron quality cuts to select the $Z^0 \rightarrow e^+e^-$ decays. These cuts also accept a small number of background events, $N_{\text{background}}$, which are adjusted for. However, the cuts exclude some Z^0 events, and this is accounted for by the efficiency, ϵ. Finally, the number of events is related to the cross section by the integrated luminosity of the data sample, $\mathcal{L}$.

This thesis is organized as follows. Chapter 2 presents a theoretical summary for Z^0 production in $\bar{p}p$ collisions. Chapter 3 describes the CDF detector, with details regarding the measured quantities that distinguish electrons from other particles. Chapter 4 describes the reconstruction of the CDF data into useful electron quantities. Chapter 5 describes the selection of events, estimation of background, calculation of selection efficiency and measurement of the collider luminosity that culminates in a value for $\sigma \cdot \mathrm{B}(\mathrm{Z} \rightarrow \mathrm{e}^+\mathrm{e}^-)$.

Chapter 2

Theoretical Expectations for $\bar{p}p \rightarrow Z^0 \rightarrow e^+e^-$ Production

2.1 The Standard Model

The Standard Model of the electroweak interaction[1] is a gauge theory built from the model of Yang-Mills [8] with an SU(2)×U(1) symmetry. Through the Higgs mechanism of spontaneous symmetry breaking [9] the gauge fields are separated into a massless photon and the massive weak bosons W^+, W^- and Z^0. The weak coupling constant (G_F) of Fermi's theory [10] is replaced by the massive propagators of the weak bosons. However, it is still useful to express the Standard Model couplings in terms of G_F; this is the notation we will use. To account for low energy phenomena, the weak boson masses must be many times the mass of the proton. In fact, the Standard Model predicts the masses in terms of the Fermi coupling, electromagnetic coupling α_{EM} and the weak (or Weinberg) angle θ_W:

$$M_W^2 = \frac{\pi\sqrt{2}\alpha_{\mathrm{EM}}}{2G_F \sin^2\theta_W} \tag{2.1}$$

$$M_Z^2 = \frac{M_W^2}{\cos^2\theta_W}. \tag{2.2}$$

The weak angle has been measured by several methods; the most important in determining the world average of .230 ± .005 is deep inelastic neutrino scattering [11]. The CDF experiment has also measured $\sin^2\theta_W$ in two ways: 1) from direct measurement of the W and Z^0 masses we obtain .233 ± .008 [12] and 2) from the charge asymmetry of Z^0 decays we obtain .230 ± .016 [13].

2.2 The Parton Model

Deep inelastic scattering revealed the existence of quasifree pointlike spin 1/2 constituent particles (partons) in the proton. These and other experiments eventually amassed a conclusive body of evidence that partons were the SU(3) quarks that Gell-Mann and Zweig had proposed as theoretical constructs to describe the spectrum of hadrons. Applying sum rules to the momentum distributions of the charged partons indicated the presence of a neutral parton, which was identified as the gluon. The parton model is used to calculate cross sections by separating a reaction into a fundamental cross section involving quarks and gluons and probability distribution functions for finding quarks and gluons inside the hadron. In proton-antiproton collisions this is expressed as:

$$\sigma = \sum_{a,b} C_{a,b} \int_0^1 dx_a \int_0^1 dx_b \;\; \hat{\sigma} \cdot [f_p^a(x_a, q^2) f_{\bar{p}}^b(x_b, q^2) + f_p^b(x_b, q^2) f_{\bar{p}}^a(x_a, q^2)], \tag{2.3}$$

where the sum is over parton species ($a, b = u, \bar{u}, d, \bar{d} \ldots t, \bar{t}, g$), $C_{a,b}$ is a color factor, x is the longitudinal momentum fraction of the parton, $\hat{\sigma}$ is the fundamental cross section and $f_p^a(x_a, q^2)$ is the probability for finding parton-a in the proton with momentum fraction x_a. In the QCD improved parton model, the distribution functions are modified by the radiation of gluons; this leads to their dependence (Altarelli-Parisi evolution [15]) on the momentum transfer, q^2.

The reactions we are interested in are broadly classified as the Drell-Yan process [14]. This is the annihilation of quarks to form an intermediate vector boson, in our case the Z^0 or γ^*. The parton momenta are constrained to form an invariant mass $\sqrt{\hat{s}}$ through the relation:

$$\hat{s} \;=\; x_a x_b s \;=\; q^2. \tag{2.4}$$

The fundamental cross section, $\hat{\sigma}$, is calculated using field theory. The parton distribution functions have been determined experimentally from several processes:

$$\begin{array}{rccc} \text{Deep inelastic scattering:} & \mu N & \rightarrow & \mu X \\ & \nu N & \rightarrow & \nu X \\ \text{Direct photon:} & pp & \rightarrow & \gamma X \\ \text{Drell Yan:} & pN & \rightarrow & \mu^+\mu^- X \end{array}$$

Several groups have extracted parton distribution functions from single experiments or global fits to several experiments. The distribution functions are published with a specification of the renormalization scheme and scales used. To manage the singularities from gluon emission a consistent renormalization scheme must be used in calculating beyond lowest order; the fundamental cross section must be calculated in the same framework as the parton distributions. The documentation of a higher order calculation will quote the renormalization scheme used; the most common is $\overline{\mathrm{MS}}$ [16].

These experiments also determine the strong coupling constant, α_s. It is conventional to quote α_s in terms of the scale parameter $\Lambda_{\mathrm{QCD}}^{(N_f)}$ and N_f, the number of participating flavors. The running of α_s is specified by the renormalization group expansion:

$$\alpha_s = \frac{12\pi}{(33 - 2N_f)\ln(\frac{q^2}{\Lambda^2_{\mathrm{QCD}}})} + \ldots. \tag{2.5}$$

The subscript of Λ_{QCD} is usually used to label the renormalization scheme employed, e.g. $\Lambda_{\overline{\mathrm{MS}}}$.

The lowest order Feynman diagram for Z^0 production is shown in figure 2.1a; this is referred to as the Born level. There are large corrections to this theoretical prediction if we account for the diagrams where the quarks radiate gluons, as in figure 2.1b-f. This introduces the *K-factor* which describes the ratio of the actual cross section to the Born-level cross section. The K-factor was initially quoted as the ratio of experimentally observed dilepton cross sections to the Born calculation. It is now also used to quote the ratio of higher order calculations to the Born level result. Although the complete order α_s correction cannot be expressed as a single factor, one can use an approximation where the largest term is factored out:

$$K \approx 1 + \frac{\alpha_s}{2\pi}\frac{4}{3}\left(1 + \frac{4}{3}\pi^2\right) \approx 1 + \frac{\alpha_s 8\pi}{9}. \tag{2.6}$$

For Z^0 production, $\alpha_s(q^2 = M_Z^2) \simeq .11$ and the above approximation indicates a sizeable correction of 30%.

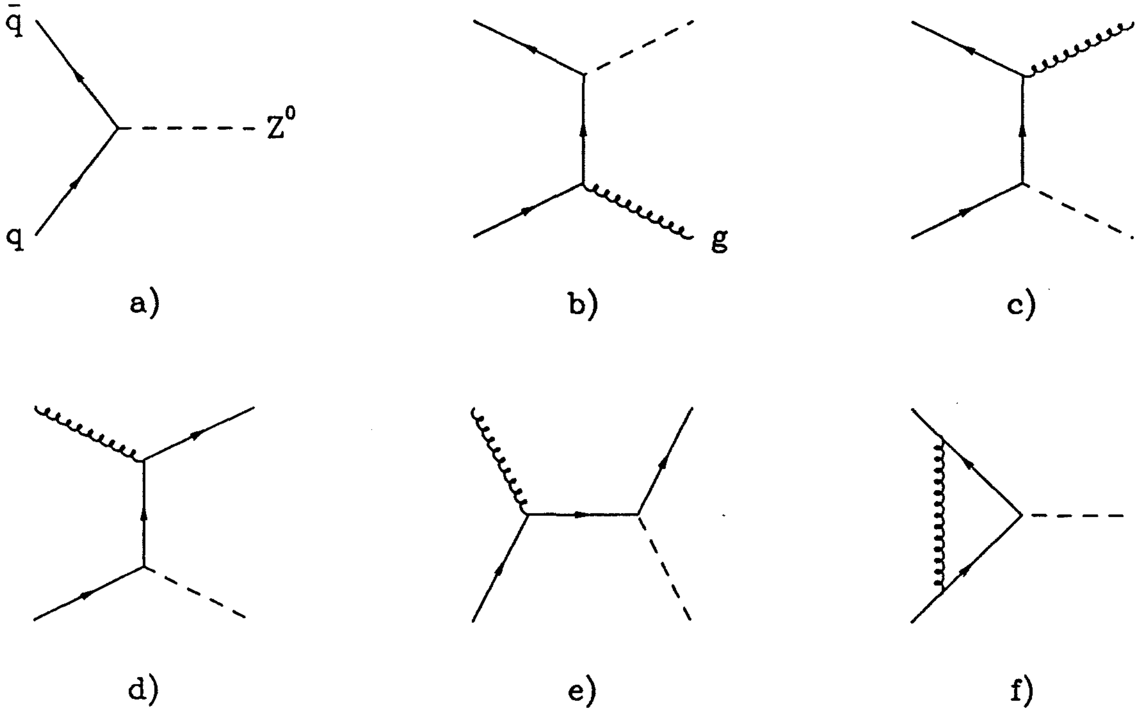

Figure 2.1: Diagrams to order α_s for Z^0 production.

2.3 The Total Cross Section for $\bar{p}p \to Z^0$ Production

Using the lowest order diagram of figure 2.1a, the parton-level cross section is:

$$\hat{\sigma}(q\bar{q} \to Z^0) = \frac{8\pi G_F}{\sqrt{2}}[(g_V^q)^2 + (g_A^q)^2] M_Z^2 \, \delta(\hat{s} - M_Z^2). \tag{2.7}$$

The fermion couplings to the Z^0 are given by $g_V^f = \frac{1}{2}(T_f^3)_L - Q^f \sin^2\theta_W$ and $g_A^f = -\frac{1}{2}(T_f^3)_L$ where $(T_f^3)_L$ is the third component of weak isospin and Q^f is the electric charge of the fermion. The values are listed in table 2.1. The color factor for quark annihilation is 1/3 (average over the initial color states and sum over the final color states). Integrating 2.3 with the DFLM-1 distribution functions[17] we find a Born-level cross section of 4.96 nb.

The next-to-leading order calculation uses the diagrams of figure 2.1b-f. The calculation has been done, using the $\overline{\text{MS}}$ scheme, DFLM-1 parton distributions and α_s determined with $\Lambda_{\overline{\text{MS}}}^{(5)} = 170$ MeV [18] [19]. The order α_s result is 6.07 nb. The uncertainty in this calculation is estimated to be ±10% from higher order diagrams, ±3% from structure function uncertainties and ±3% from uncertainty in the W mass.

fermion	$(T^3_f)_L$	Q^f	g_V	g_A
u, c, t	$\frac{1}{2}$	$\frac{2}{3}$	$\frac{1}{4} - \frac{2}{3}\sin^2\theta_W$	$-\frac{1}{4}$
d, s, b	$-\frac{1}{2}$	$-\frac{1}{3}$	$-\frac{1}{4} + \frac{1}{3}\sin^2\theta_W$	$\frac{1}{4}$
ν_e, ν_μ, ν_τ	$\frac{1}{2}$	0	$\frac{1}{4}$	$-\frac{1}{4}$
e, μ, τ	$-\frac{1}{2}$	-1	$-\frac{1}{4} + \sin^2\theta_W$	$\frac{1}{4}$

Table 2.1: The couplings of the Z^0 to fermions.

Another group has also done the calculation, including some of the diagrams of order α_s^2 [20]. They use the DIS scheme, DFLM-4 parton distribution functions and α_s determined with $\Lambda^{(5)}_{\overline{\mathrm{MS}}} = 200$ MeV. This paper predicts a total cross section of 6.16 nb for the order α_s calculation and 6.78 nb for their partial order α_s^2 calculation.

Figure 2.2 shows the theoretical Z^0 cross section as a function of $\sqrt{s}$ for $\bar{p}p$ collisions. Solid curves are plotted for the Born level, order α_s and order α_s^2 calculations of reference [20]. A dashed curve is plotted for the order α_s calculation of reference [19].

2.3.1 The Branching Ratio for $Z^0 \rightarrow e^+e^-$

Our measurement will only include the e^+e^- final state. At lowest order, the branching ratio for $Z^0 \rightarrow e^+e^-$ is determined from the partial width:

$$B = \frac{\Gamma^Z_{ee}}{\Gamma^Z_{tot}} = \frac{\Gamma(Z^0 \rightarrow e^+e^-)}{\sum\limits_f \Gamma(Z^0 \rightarrow f\bar{f})}, \tag{2.8}$$

where

$$\Gamma(Z^0 \rightarrow f\bar{f}) = \frac{\sqrt{2}G_F M_Z^3}{3\pi}[(g_V^f)^2 + (g_A^f)^2]. \tag{2.9}$$

More sophisticated predictions are made taking into account the mass of the decay fermions and higher order corrections. The standard model prediction for the total width, Γ^Z_{tot}, is 2.500 ± .042 GeV; for the width into electrons, Γ^Z_{ee}, it is .0838 ± .0009 GeV [21]. From these numbers, we calculate a branching ratio of .0335 ± .0005. Note, the uncertainty of .0005 is probably an overestimate, since the calculation of Γ^Z_{tot} and Γ^Z_{ee} includes common

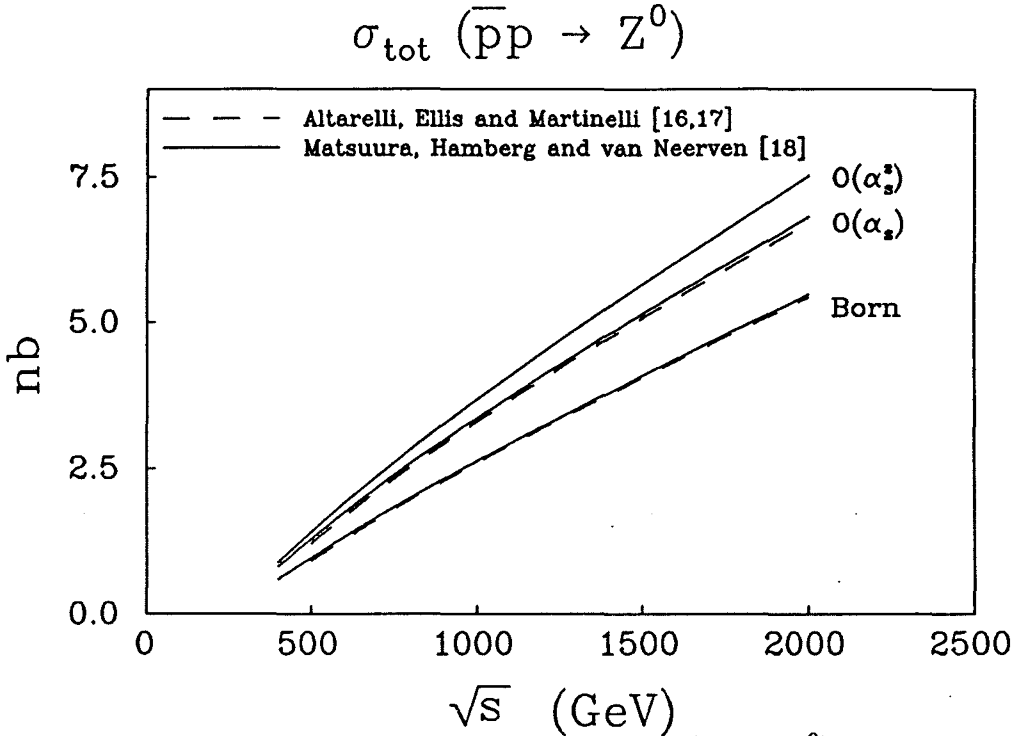

Figure 2.2: Born level and higher order calculations of $\sigma_{tot}(\bar{p}p \rightarrow Z^0)$ as a function of center-of-mass energy.

parameters. In any case, the uncertainty in the branching ratio is negligible compared to the uncertainty in the cross section for predicting our measured quantity, $\sigma \cdot B$. The values of Γ^Z_{tot} and Γ^Z_{ee} have been measured at LEP; the average results are: $\Gamma^Z_{tot} = 2.538 \pm .028$ and $\Gamma^Z_{ee} = .0829 \pm .0016$ [21].

Using the standard model prediction for the branching ratio into electrons, the theoretical predictions for $\sigma \cdot B(Z^0 \rightarrow e^+e^-)$ at $\sqrt{s} = 1800$ GeV are:

Born		166 pb
Order α_s	[18] [19]	203 pb
Order α_s	[20]	206 pb
Order α_s^2	[20]	227 pb

2.4 The Mass Spectrum of e^+e^- Production

In the above section we treated the Z^0 as a delta function, because this is the preferred theoretical comparison for the total cross section. But we experimentally observe a spectrum of e^+e^- masses produced by virtual photon and Z^0 decay. The parton model calculation is therefore done with three terms: one for the γ^*, one for the Z^0 and an interference term. The propagators for the bosons are now explicit:

$$\begin{aligned}\frac{d\sigma}{dM^2} \equiv \frac{d\sigma}{dq^2} = & \sum_{a,b}\frac{1}{3}\int_0^1 dx_a \int_0^1 dx_b \, [f_p^a(x_a) f_{\bar{p}}^b(x_b) + f_p^b(x_b) f_{\bar{p}}^a(x_a)] \quad \times \\ & \left[\frac{4\pi\alpha_{\text{EM}}^2}{3q^2}(Q^a)^2 \right. \quad + \\ & \frac{16}{3\pi}\left(\frac{G_F M_Z^2}{\sqrt{2}}\right)^2 \frac{q^2\,[(g_V^e)^2+(g_A^e)^2]\,[(g_V^a)^2+(g_A^a)^2]}{(q^2-M_Z^2)^2+M_Z^2\Gamma_Z^2} \quad + \\ & \left.\frac{16}{9}\left(\frac{G_F M_Z^2}{\sqrt{2}}\right)\frac{g_V^e g_V^a Q^e Q^a (q^2-M_Z^2)}{(q^2-M_Z^2)^2+M_Z^2\Gamma_Z^2}\right]. \end{aligned} \qquad (2.10)$$

The differential cross section $d\sigma/dM$ is shown in figure 2.3. We use this calculation to correct our observed number of events for the contribution from Drell-Yan γ and $\gamma \cdot Z$ interference. We integrate the contribution from all three terms between 75 and 105 GeV. We separately integrate the contribution from the Z^0 term alone, from 75 to 105 GeV. Integrating this fundamental cross section with DFLM-1 structure functions yields a ratio of:

$$f_{DY} = \frac{\int_{75}^{105} \sigma_Z dM}{\int_{75}^{105} \sigma_{Z+Z\gamma+\gamma} dM} = .987. \qquad (2.11)$$

We use this factor to multiply the number of events observed to obtain the effective number of events due to the Z^0 term. For 254 events, this is equivalent to a background subtraction of 3.3 ± 1 events. Note: we account for Z^0 events that fall out of our 30 GeV mass window in our definition of acceptance (see section 5.2).

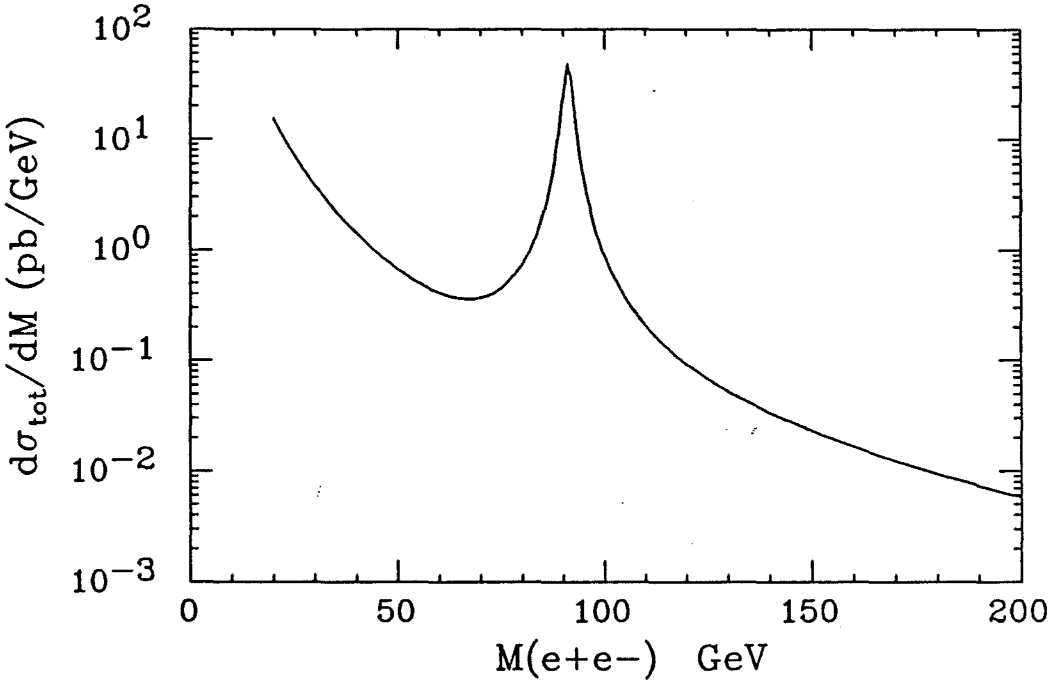

Figure 2.3: $d\sigma/dM$ for $\bar{p}p \rightarrow e^+e^-$.

Chapter 3

The CDF detector

3.1 Introduction

The CDF detector is described in detail in a special edition of Nuclear Instruments and Methods [22]. The CDF detector is shown isometrically in figure 3.1a and in cross section in figure 3.1b. The detector is a general purpose 4π detector with cylindrical symmetry designed and segmented appropriately for electron, muon and jet identification. It is divided along the beam axis into central (C), plug (P) and forward (F) regions. We classify dielectron events by the region that each electron is detected in, e.g. an event with a central electron and a plug electron is classified as C-P. Each region has a unique combination of tracking and calorimetry coverage that will be discussed below. However, there are definitions common to each region that we described first.

The CDF coordinate system is defined in cartesian coordinates as having the $+z$ axis along the anti-proton direction, with $+x$ pointing out of the ring, parallel to the ground and $+y$ pointing vertically. This sets the cylindrical coordinates so that $\theta = 0$ is pointing along the $+z$ axis and $\phi = 0$ is along the $+x$ axis. It is the convention that detector logical addresses increase with polar angle, θ and azimuthal angle, ϕ. The $+z$ axis also points west, and it is common to refer to the detector halves in terms of East and West.

Along the beam axis, the calorimetry is segmented on a scale that is well matched to the general characteristics of hadronic collisions. This measure is pseudorapidity and is defined

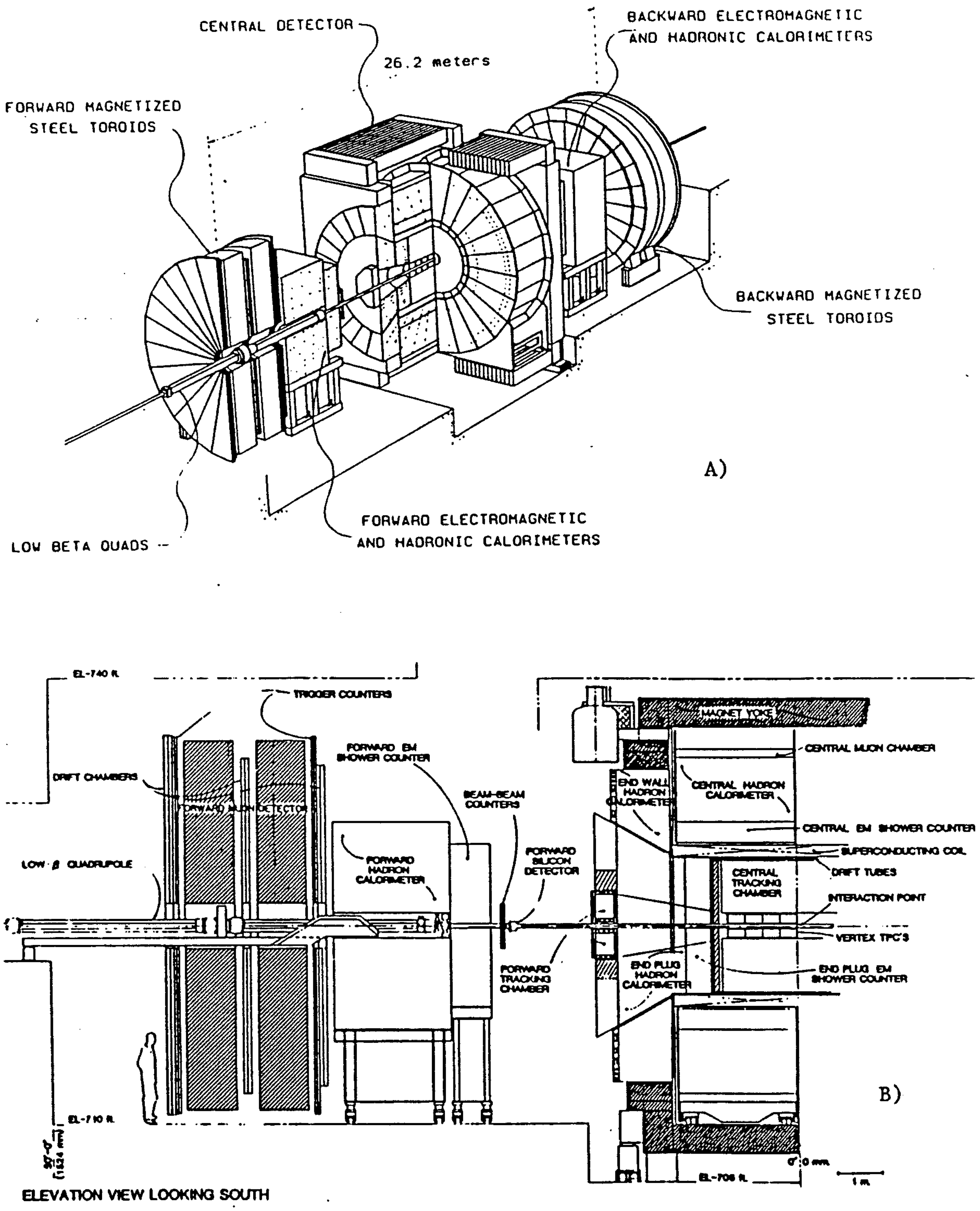

Figure 3.1: The CDF detector. A: Isometric view of detector as installed in collision hall. B: Cross section of detector of 1/2 of the detector.

as:

$$\eta = -\ln \tan \frac{\theta}{2}. \tag{3.1}$$

For high p_t, low mass particles, pseudorapidity is a good approximation of a particle's true rapidity:

$$y = \frac{1}{2} \ln \frac{E + p_z}{E - p_z}. \tag{3.2}$$

Because rapidity transforms additively under Lorentz transformations, the detector geometry is approximately invariant for the z-boosts that are an inescapable consequence of $\bar{p}p$ collisions. In minimum bias events, the average number of particles per unit pseudorapidity is approximately constant. Also, segmenting the calorimetry in units of constant η and ϕ also provides a natural view of jets, such that their local transverse energy distribution is on average circular. The calorimetry is arranged with projective geometry, with the nominal collision point at its focus. The size of each tower is also matched to the transverse size of an electromagnetic shower, which provides a useful criterion for electron identification.

3.2 The Central Region

3.2.1 Overview

The central region covers η from -1.1 to $+1.1$. A particle propelled outward from a $\bar{p}p$ collision first traverses a thin walled beryllium section of the beam pipe. It goes through the Vertex Time Projection Chamber. This device provides the z-vertex of the interaction and also yields tracking information that is especially important at lower angles; the details of this detector will be discussed in a later section. The most important tracking information for central particles is measured by the Central Tracking Chamber, with momentum determination in a 1.4 T magnetic field generated by a large superconducting solenoid. Outside of the tracking detectors, a particle next encounters electromagnetic and then hadronic calorimeters. Finally, drift tubes are located beyond the calorimetry to identify muons.

3.2.2 The Central Tracking Chamber (CTC)

The CTC is a large volume wire chamber that reconstructs charged tracks with excellent detail. The total number of wires is 36,504, which includes potential wires between each sense wire. The wires are grouped into 9 *superlayers.* Five of the superlayers have 12 sense wires that run parallel to the beam and the magnetic field. Between each of these axial layers are four stereo superlayers of 6 sense wires each. The stereo wires are strung at a 3° angle from the beam; this yields a z-position resolution of 3 mm, comparable to the position resolution of the central calorimeter. A stiff track that passes through the outer radius of the CTC will have 84 hits spread over a path of at least 1 meter. The chamber has a momentum resolution (using beam constrained fits) of $\sigma_p/p = .0011p_t^2$. For isolated high p_t tracks typical of electroweak boson decay the track finding efficiency is indistinguishable from 100%. For this analysis, we shall be concerned with using the high efficiency and resolving power of the CTC to assist in identifying electrons.

Figure 3.2 shows a cross section display of a Z^0 event in the CTC. The left frame of the display shows a closeup view of a high p_t track. The wire locations are marked by fine dots and hit information is marked by thicker lines. The superlayer hits are plotted for the two ambiguous solutions although only one forms a physical track.

3.2.3 The Solenoid

The Solenoid provides a uniform magnetic field, nominally 1.5 T, for determining the momentum and charge of particles produced in the central region. The coil consists of 1164 turns of an aluminum-stabilized Nb-Ti-Cu superconductor. For the 1988 CDF run, the magnetic field was reduced from its nominal value to 1.4116 T because of a heat leak.

3.2.4 The Central Electromagnetic Calorimeter (CEM)

The CEM consists of 48 *wedges* (see figure 3.3), installed as four *arches* of 12 wedges centered on the nominal collision point. Each wedge is made of ten projective towers of 5 mm thick polystyrene scintillator alternating with 1/8 inch sheets of aluminum clad lead. Actually,

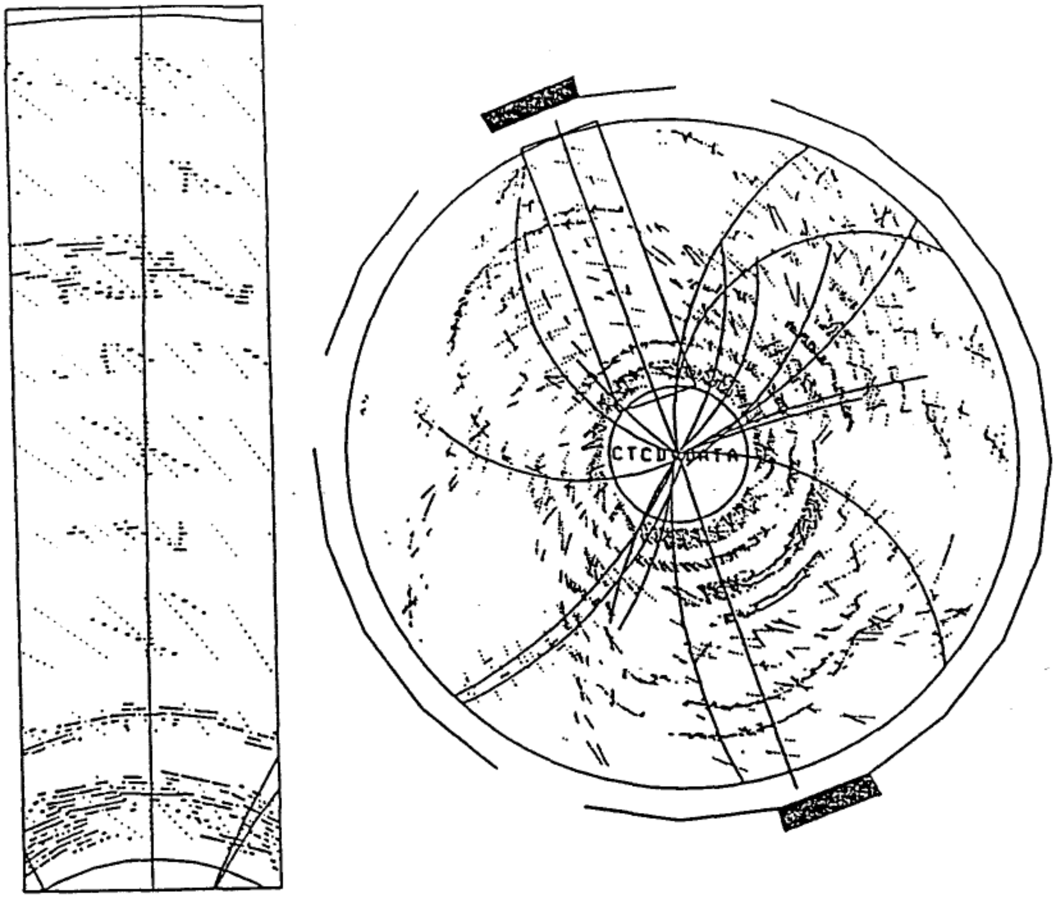

Figure 3.2: A Z^0 event as seen in the Central Tracking Chamber. An expanded view of the highest p_t track is shown to the left.

the towers at larger incident angles have some layers replaced with inactive material to tune the total number of radiation lengths to a constant value of 18 X_0. On each side of the stack of scintillator, between it and an enclosing metal can, sheets of waveshifter collect the light and transmit it to acrylic lightguides. The lightguides carry the scintillation light outward to pairs of photomultiplier tubes. Each wedge subtends 15° in azimuth and covers the polar angle from 90° to 30° or 120°. Inside each wedge, near shower maximum, is a strip chamber that provides good position resolution as well as a measure of transverse shower shape. This will be described more fully in the next section.

The wedges were calibrated in a test beam with 50 GeV electrons. The energy resolution function is:

$$\frac{\sigma_E}{E} = \frac{13.5\%}{\sqrt{E \sin\theta}} \tag{3.3}$$

All 24 wedges were calibrated at each of the tower centers. The reproducibility of calibration was studied by repeating the test beam procedure for three of the wedges at 5 week intervals;

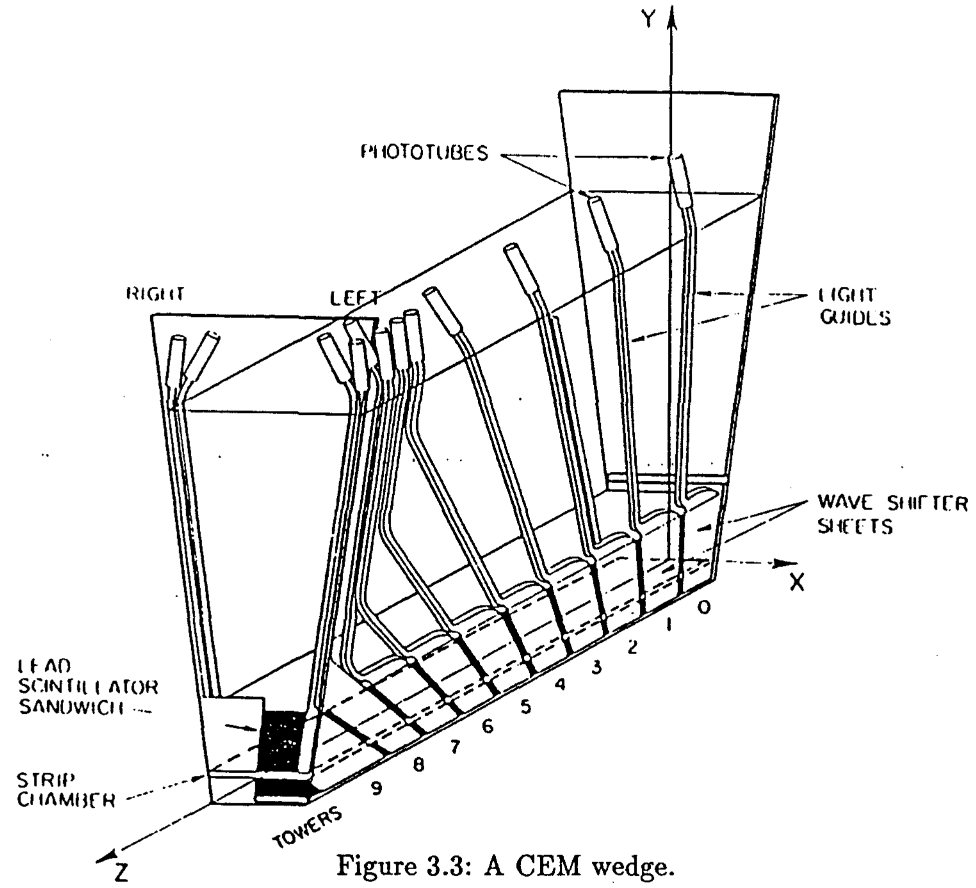

Figure 3.3: A CEM wedge.

the energy scale was reproducible to better than 1%. A detailed position scan was done on five of the wedges to determine a systematic response map that is used to correct the data from all of the wedges. A 6% peak-to-peak map was measured that reflects 1) shower leakage at the edges of the calorimeter and 2) variations in light collection due to attenuation in the scintillator, position in the wave shifter and details of the tower boundaries (see figure 4.1). In situ energy calibration was done using the agreement between calorimeter energy and tracking momentum (section 4.3).

3.2.5 The Central Electromagnetic Strip Chamber (CES)

Each CEM wedge has a gas proportional strip chamber located at shower maximum ($r =$ 184.15 cm from the beamline). This chamber is used to determine the position and shape of the electromagnetic shower. The CES information is used in three ways to help identify electrons: 1) the transverse shape in the z-strips is compared to a shower parametrization to calculate a χ^2 test, 2) the CES z and ϕ position is used in track-shower matching and

3) the CES z position is used to predict the transverse energy sharing of the EM towers, which is compared to the EM data to form a quality variable.

In the ϕ-view, the CES consists of 64 wire channels that subtend $\pm 7°$ in ϕ (out of $\pm 7.5°$ per wedge). The wires are read out in pairs, with a logical separation of 1.45 cm. Each wedge has two z segments of wire plane: the first covers z from 6.16 to 121.16 cm (towers 0-4), the second covers z from 121.16 to 239.56 (towers 5-9). The z-view is read out by cathode strips. The wire plane covering towers 0-4 has a strip width of 1.67 cm; the wire plane covering towers 5-9 has a strip width of 2.01 cm.

3.2.6 The Central and Endwall Hadronic Calorimeters (CHA and WHA)

Following the CEM, each wedge has steel and scintillator hadronic calorimetry built with a similar light collection and readout design. The innermost 6 towers of the CEM are backed up by 6 towers of hadronic calorimetry totally contained in the wedge (CHA). To maintain the projective geometry, a transition is necessary at the extreme edges of the central cylinder. Mounted on the outside of the wedges and the magnet yoke are more 15° segments of steel and scintillator calorimetry (WHA). The next 3 CEM towers are backed up by a combination of layers in the CHA and layers in the WHA. The last CEM tower and the outer two towers of the plug EM calorimeter are backed up by the WHA. The hadron calorimeters are important to electron identification because they record leakage of energy from the EM compartment. To select electrons and reject pions, we cut on the ratio of hadronic energy to EM energy.

3.3 The Plug Region

3.3.1 Overview

The plug region covers $|\eta|$ values from 1.1 to 2.4. It consists primarily of planes of gas calorimetry, again in projective towers, that fit in each end of the central cylinder like a cork. The outer angle is approximately 30° and around the beampipe is a 10° hole through which particles escape to the forward region detectors. There is some tracking coverage from the CTC, although the tracks necessarily exit the CTC end-plate and may not have hits in every superlayer. However the VTPC is most efficient at these angles and can provide good track identification. There is no muon detector coverage in this region.

3.3.2 The Vertex Time Projection Chamber (VTPC)

The VTPC is a series of eight octagonal modules strung along the beampipe and filling the inner radius of the CTC (27.7 cm). Each module consists of a central high voltage grid, a drift space of 15.25 cm on each side of the grid, and proportional chamber readout capping each end of the module. The endcaps are arranged in octants with sense wires and cathode pads. From the arrival times at the sense wires, tracks may be reconstructed in the $r-z$ plane. Adjacent modules are rotated by half an octant, which eliminates inefficiencies at the octant boundaries and also provides stereo information for determining the ϕ position. In some modules the wires and pads are instrumented with pulse-height readout that can provide an independent method to reconstruct three-dimensional tracks. An important role of the VTPC is to provide the initial reconstruction of the event vertex, especially in the context of multiple interactions which are present at high luminosities. It is constructed with the lightest possible materials to minimize photon conversions, and by recording the absence of charged tracks it can play a major role in the rejection of conversions that occur at the VTPC-CTC boundary. But for this analysis its primary role is in identifying charged tracks that extrapolate to plug and forward electromagnetic clusters.

3.3.3 The Plug Electromagnetic Calorimeter (PEM)

Two PEM calorimeters fit inside the ends of the central arches; one on each side of the collision axis. They subtend polar angles from 10° to 30°, which covers particles that exit the CTC endplate. The calorimeter consists of 34 layers of resistive plastic proportional tubes alternating with lead sheets. The total radiation length is 18-21 X^0 depending on angle of incidence. The tubes are bonded to G10 upon which a copper cathode pad structure is etched. The pad structure is ganged to form projective towers. Each tower is divided

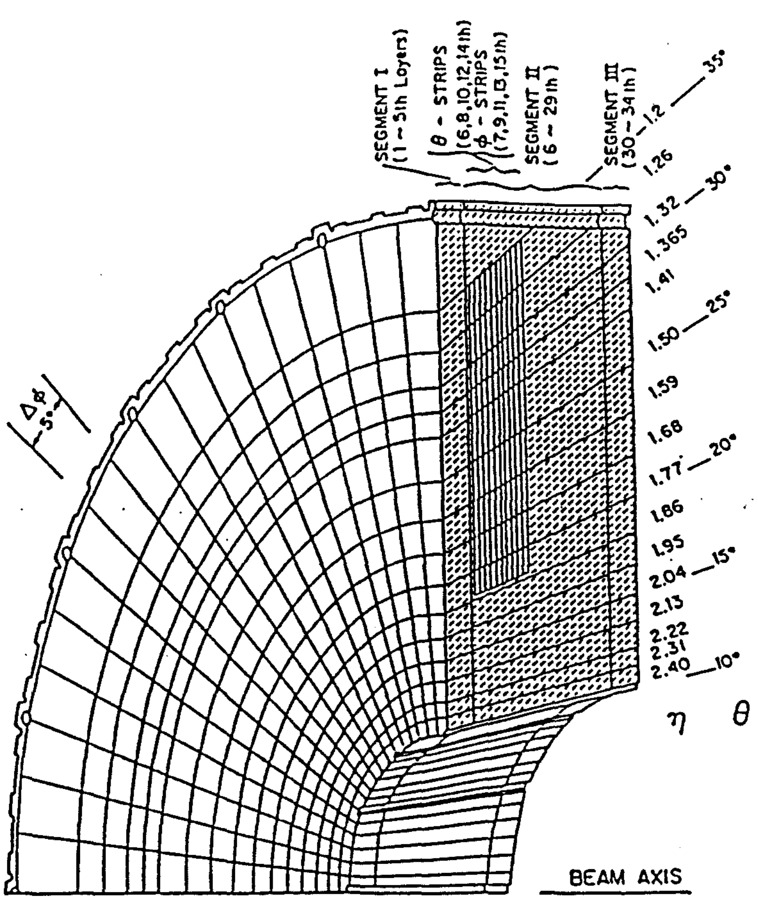

Figure 3.4: A PEM quadrant

into three depths of 5, 24 and 5 layers that provide a longitudinal description of the shower that can be useful in electron identification. A PEM quadrant is shown in figure 3.4.

The PEM was studied in a Fermilab test beam with 20-200 GeV electrons. The energy resolution was determined to be:

$$\frac{\sigma_E}{E} = \frac{28\%}{\sqrt{E}} \tag{3.4}$$

The response was approximately linear, with a quadratic component of -7% at 200 GeV at 1.7 kV. The longitudinal and transverse development of showers was also studied and chi-squared shape algorithms were developed to assist in identifying electrons.

3.3.4 The Plug Electromagnetic Strips (PES)

The strip chambers surrounding shower maximum provide both an improved measure of position as well as a fine view of the transverse shape of the shower that can be used in selecting electrons. The ten chambers 6-15 have the side opposite the cathode pads clad with fine strips of cathode to provide better position and shape resolution. The even numbered layers have arc shaped strips of width $\delta\eta = .02$. The odd numbered layers have radial strips of width $\delta\phi = 1°$. The position resolution of the strip chambers is .05° in the θ-direction and .1° in the ϕ-direction. The strip chambers extend from $\eta = 1.2$ to $\eta = 1.86$; beyond this, the cathode pad structure is fine enough to resolve an electromagnetic shower.

3.3.5 The Plug Hadronic Calorimeter (PHA)

The PHA is also constructed of resistive plastic tubes with cathode pad readout. The pad structure forms projective towers that line up with those in the PEM. The PHA was calibrated in the testbeam along with the PEM. Its primary role in electron analysis is to record the absence of energy leakage from the PEM.

3.4 The Forward Region

3.4.1 Overview

The forward region covers $|\eta|$ values from 2.4 to 4.2, which roughly corresponds to 10° to 2°. The calorimetry begins 6.5 meters from the interaction point. This separation allows the unit cell of $2\pi/72$ by .1 to project to pad sizes of 3 to 30 cm, for the innermost and outermost pads respectively. The forward calorimeters on each end of the collision axis are divided into four 90° quadrants of gas calorimetry. There are 30 layers of lead and proportional chamber EM calorimetry followed by 27 layers of steel and proportional chamber hadron calorimetry. The total radiation length of the EM calorimeter is approximately 25 X^0. Tracking coverage is provided by the VTPC down to $|\eta| = 3.5$. Behind the calorimetry are large muon toroids and muon detection chambers.

3.4.2 The Forward Electromagnetic Calorimeter (FEM)

The active region of an FEM chamber is comprised of a series of 124 rectangular proportional tubes where three sides are aluminum U-channels and the fourth side is the cathode pad readout. The cathode pad structure is etched in copper on the outer side of a fiberglass panel. The inner side of the panel is coated with resistive epoxy and bonded to the U-channels (.7 cm deep by 1 cm wide) to form an enclosed gas volume around a 50 μm wire.

The resistive epoxy drains off the surface build-up of positive ions that would accumulate from showers, but slowly enough ($\tau \sim 50$ μsec) that the charge integration of a single event may take place.

Test beam studies were performed on four of the eight FEM quadrants in 1985 and a fifth was studied in 1986. The 1986 testbeam had a complete replica of the electronics, gas gain monitoring and data acquisition used in the colliding beam experiment and provided the energy scale calibration used for this data. Corrections to the energy scale were derived from the data, using the Z^0 mass as a calibration. The earlier test beam provided important studies in energy resolution, energy response, position resolution and shower shapes. The resolution function for the FEM is

$$\frac{\sigma_E}{E} = \frac{25.4\%}{\sqrt{E}} + .5\% \tag{3.5}$$

The energy response is approximately linear from 0-100 GeV, but a non-linear component is evident at higher energies (10% at 200 GeV). Beam wire chambers provided an independent measure of the position of test beam electrons and afforded studies of position resolution. Depending on whether a shower is in large or small pads and how close it is to a pad boundary, the position resolution ranges from .1 to .4 cm.

3.4.3 The Forward Hadronic Calorimeter (FHA)

The chambers of the FHA are constructed nearly identically to those of the FEM. The proportional tube cell size is 1 cm deep by 1.5 cm wide and overall the chambers are somewhat larger. The energy resolution for single pions is approximately $140\%/\sqrt{E}$.

3.5 The Trigger

3.5.1 The Beam-Beam Counters (BBC)

A plane of 16 scintillation counters is mounted on the front face of each forward calorimeter to record the low angle particles from beam-beam collisions and provide the first level of event triggering. They form a rectangular frame around the beam pipe, extending from

$\eta = 3.24$ (4.47°) down to $\eta = 5.90$ (.32°). The minimum bias trigger requires at least one counter at each end of the collision to fire within a 15 ns window centered on the beam crossing.

3.5.2 The Multi-Level Trigger Hardware and Software

The CDF trigger is divided into four parts:

- Level 0 requires BBC hits on each side of the interaction region within 15 ns of the beam crossing.
- Level I is a simple comparator of the calorimeter energy. For the Level I and II decisions, fast output signals from the front-end electronics are provided that are ganged into trigger towers with width $\delta\eta = 0.2$ and $\delta\phi = 15°$. The trigger towers are weighted by $\sin\theta$ to represent transverse energy.
- Level II uses hardware cluster finders and hardware track processors to set further criteria.
- Level III executes FORTRAN-77 algorithms on the final data stream and makes the last decision before writing the event to tape. The Level III reconstruction code is a subset of the offline production code and runs on the fully digitized data in the same format that is written to tape.

For this analysis, the most important trigger is the ELECTRON_12 Trigger. It begins with a Level I requirement of 6 GeV in a single CEM trigger tower. In Level II, CEM trigger clusters are formed beginning with a seed trigger tower that has $E_t > 4$ GeV. Adjacent trigger towers are added to the cluster if their energy is at least 3.6 GeV. The transverse energy including the hadronic compartment is separately tabulated and the ratio of total E_t to EM E_t must be less than 1.125. The E_t of this trigger cluster must be greater than 12 GeV. Finally, the hardware track processor must match a track in the ϕ-view with $p_t > 6$ GeV.

Much of the data was taken requiring only the Level II decisions. During the latter part of the run the Level III algorithm was introduced. It uses the finer segmentation available in the raw data to calculate the a lateral energy sharing variable (see section 4.4). It also applies a more sophisticated tracking algorithm to harden the 6 GeV p_t threshold.

Chapter 4

Data Reconstruction

4.1 Transverse Energy Reconstruction

The reconstruction of an electron candidate begins with the measurement of energy in the calorimeter. The readout hardware corrects for pedestal offset and electronics gain online. The rest of the reconstruction occurs in offline computer analysis. First, corrections are made for small pedestal shifts in some channels. The raw datum (ADC counts proportional to the charge deposited) for each tower is scaled by one overall factor per detector to determine a tower energy in GeV. The array of tower energies is then searched to identify and eliminate noise, which may come from several sources:

- Single phototube noise is caused by particles showering in the lightguides or by high voltage discharge at the phototube. For a real EM shower, there is significant signal in both of the phototubes that read out a tower. This noise is eliminated by disregarding towers where there is a large signal in only one phototube.
- Discharge spikes are present in the outer perimeter of the PEM. This noise is caused by high voltage leakage at the proportional tube ends. The spikes are identified by nearly 100% of the tower energy being in one depth segment and the wire profile dominated by a single layer with a large signal that roughly matches the tower energy.
- Gas spikes are caused by low energy neutrons associated with the hadronic showers. The neutrons penetrate the calorimeter and knock loose protons from molecules in

the gas calorimeters. The proton ranges out in a single tube and generates a large signal in a single layer and tower. The low energy end of this spectrum contributes to the energy fluctuations of hadronic jets; however there is a high energy tail that is unphysical in that the reconstructed energy in a spike exceeds the energy of any particle in a jet. This signature is very similar in appearance to discharge spikes and is eliminated by the same algorithm.

- Cable noise is purely electronic and is associated with ground loops in the cables running from the gas calorimeter pads to the front end electronics. This noise is only significant in the hadronic calorimeters. It appears as a group of several towers with large signals, with the group of towers corresponding to a ribbon cable. There is no corresponding signal in the wires. It is eliminated by an algorithm that identifies this signature while still being $> 99\%$ efficient for hadronic jets.

A primary event vertex is identified using the VTPC data. Straight line tracks are found in the $r-z$ projection and are extrapolated to the beam axis. We then search for the largest clusters of points where the tracks intersect the beam axis. An array of tower transverse energies is formed by weighting the tower energy by $\sin\theta$, where θ is the polar angle to the tower center measured from the primary event vertex. Note: for the final determination of a CEM electron E_t, the track associated with the electron is used to calculate $\sin\theta$.

4.2 Energy Clustering

The electron clustering is a nearest-neighbor algorithm with limited cluster size. The array of EM tower E_t is sorted and searched for seed towers greater than 3 GeV. Neighboring towers (sharing an edge or a corner with any tower in the cluster) are included if the their E_t^{EM} is greater than .1 GeV; they are also marked so they can not form the seed for a subsequent cluster. The clustering stops when there are no neighboring towers above threshold or if the cluster size reaches a predetermined limit. This limit is based on the relative size of an electron shower and the tower size of each detector: in the CEM a cluster is limited to 3 towers in eta by 1 tower in phi, in the PEM the limit is 5 by 5 towers and in the FEM the limit is 7 by 7 towers.

The sum of the tower E_t in the cluster must be greater than 5 GeV for the cluster to be retained. The hadronic transverse energy in the cluster towers is also summed. The ratio E^{Had}/E^{EM} must be less than .125 for the cluster to be retained. This ratio, referred to as Had/EM, is used to select electrons in all three detector regions.

4.3 Electron Energy Correction

Several corrections are applied to get the best estimate of the CEM electron energy:

CEM Energy Corrections

- The CEM tower response has been mapped as a function of η and ϕ from a position scan of a single wedge using testbeam electrons. The response for a typical tower is shown in figure 4.1. To apply this correction in CDF data, we use the location of the CES strip clusters to determine the location of the shower in the wedge.

- The relative CEM tower-to-tower response was mapped out using $\sim$ 17000 inclusive electrons with $E_t > 12$ GeV. By matching calorimeter energy to track momentum we determine a relative response factor for each CEM tower.

- The overall CEM energy scale is tied to the CTC momentum measurement using 1800 W electrons. The CTC mass scale uncertainty is .2% as determined by a sample of J/ψ and Υ dimuons. The E/p comparison of the W electrons takes into account both bremmstrahlung using a radiative W Monte Carlo and the full detector simulation. From this an overall scale factor of 1.017 was determined.

Using these corrections, we have used 65 C-C dielectron events to measure a Z^0 mass of 91.1 ± .5 [23], in good agreement with the SLC result of 91.14 ± .12 [24] and the LEP average of 91.161 ± .031 [25].

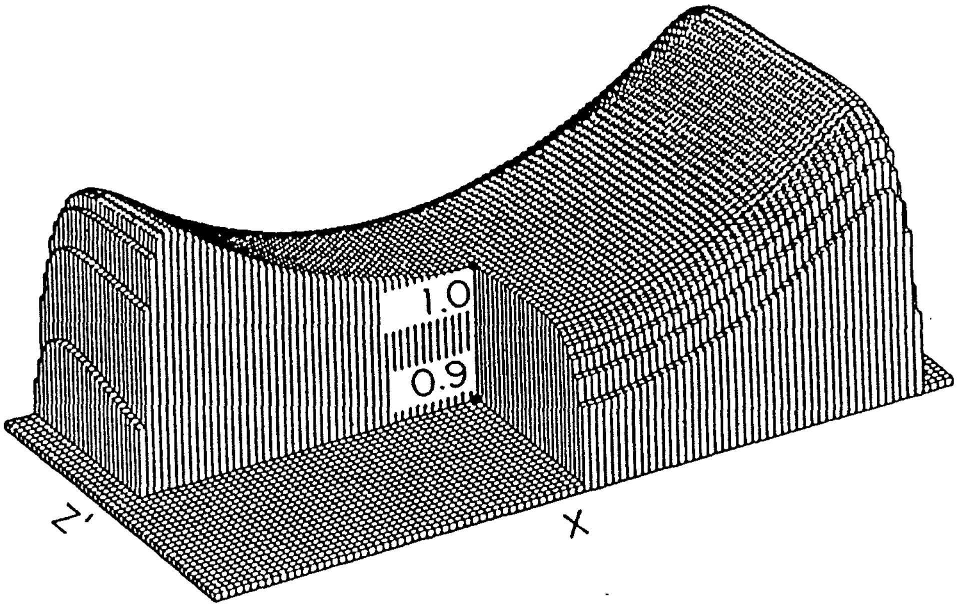

Figure 4.1: The response map of a typical CEM tower.

There are also measurement corrections to determine the best PEM and FEM electron energy:

PEM and FEM Energy Corrections

- In both gas EM calorimeters we make a correction for layers that were turned off for a given run (i.e. they had no high voltage applied). The dead layers are identified from a database of the run conditions. Using the wire energy profile an interpolation is done to account for the energy that should have been measured by the dead layer.
- The PEM calorimeter response as a function of tower in the quadrant was determined in the testbeam. No such measurement has been performed for the FEM and the relative response is assumed to be 1.0.
- The energy response of the PEM and FEM is non-linear at high energies. The PEM non-linear response was measured in the testbeam. The FEM response was measured in the testbeam up to 200 GeV. However, the energy of the forward leg of C-F Z^0 electrons extends up to 400 GeV. The extrapolation of the testbeam response was measured by studying the average C-F mass as a function of FEM electron energy

[26]. By constraining the result to the C-C mass measurement we: 1) determine the non-linear response and 2) tie the overall scale to the central region.

- **The quadrant-to-quadrant response of the PEM was determined by fixing the Z^0 mass** for C-P events in each quadrant to the mass found in a quadrant whose scale was well measured in the testbeam. The C-P Z^0 mass in this quadrant was in good agreement with the C-C Z^0 mass. The FEM quadrant-to-quadrant response was measured using a technique involving the neutron induced gas spikes [27] and was found to be in good agreement with the average Z^0 mass in each quadrant.

After making all corrections to the calorimeter energy, we then determine the best value for the direction of the electron. For CEM electrons this comes from the helical track fit to the CTC data. For PEM and FEM electrons we use the centroid of the energy deposition in the calorimeter. If the PEM electron is in a region covered by the PEM strips, we use the strip cluster position instead of the tower centroid. The electron direction is taken as a straight line pointing from the collision vertex to the calorimeter position. Using the electron direction to determine the polar angle θ, we then have the electron transverse energy: $E_t^e = E \sin\theta$.

4.3.1 Electron Isolation

A variable used for electron selection in all detectors is *isolation*. This is a measure of the energy found in the vicinity of the electron. There is a tail of hadronic jet fragmentation that fakes an electron: the jet must be very electromagnetic (from direct π^0 decay or early hadronic shower that is mostly π^0s) and in detectors where a track match is required, it must have a track pointing to the EM shower. Statistically, this tail reveals itself by the presence of jet energy nearby the fake electron.

In general, a real electron may also have significant neighboring energy; for example the electron from the semileptonic decays of b-quark will be in or near the rest of the b-jet. Even if the electron is not near a jet there is always an *underlying event* energy associated with the breakup of the proton and antiproton. However, the electrons found in W and Z^0 decay have energies well above that of the underlying event and any overlap with a jet would be accidental. Thus isolation is a variable that helps separate jets that fluctuate to fake an electron from real electrons.

The isolation of an electron is calculated by summing up the tower E_t (EM + Had) in a cone of radius .4 centered on the electron position. The CDF convention is to subtract the corrected electron E_t (the electron cluster will always be contained in a radius of .4) and then divide by the sum E_t in the cone:

$$\mathrm{Iso}(\mathrm{r} = .4) \quad = \quad \frac{\left(\sum\limits_{\mathrm{towers}}^{\mathrm{cone}} E_t\right) - E_t^e}{\sum\limits_{\mathrm{towers}}^{\mathrm{cone}} E_t}. \tag{4.1}$$

The isolation for Z^0 candidate electrons in each detector is shown in figure 4.2. The events are selected with all of the electron cuts applied (except that the Had/EM is loosened to $< .1$). In selecting our final events, we require isolation $< .1$, based on these distributions. Isolation is discussed again in section 5.3.3.

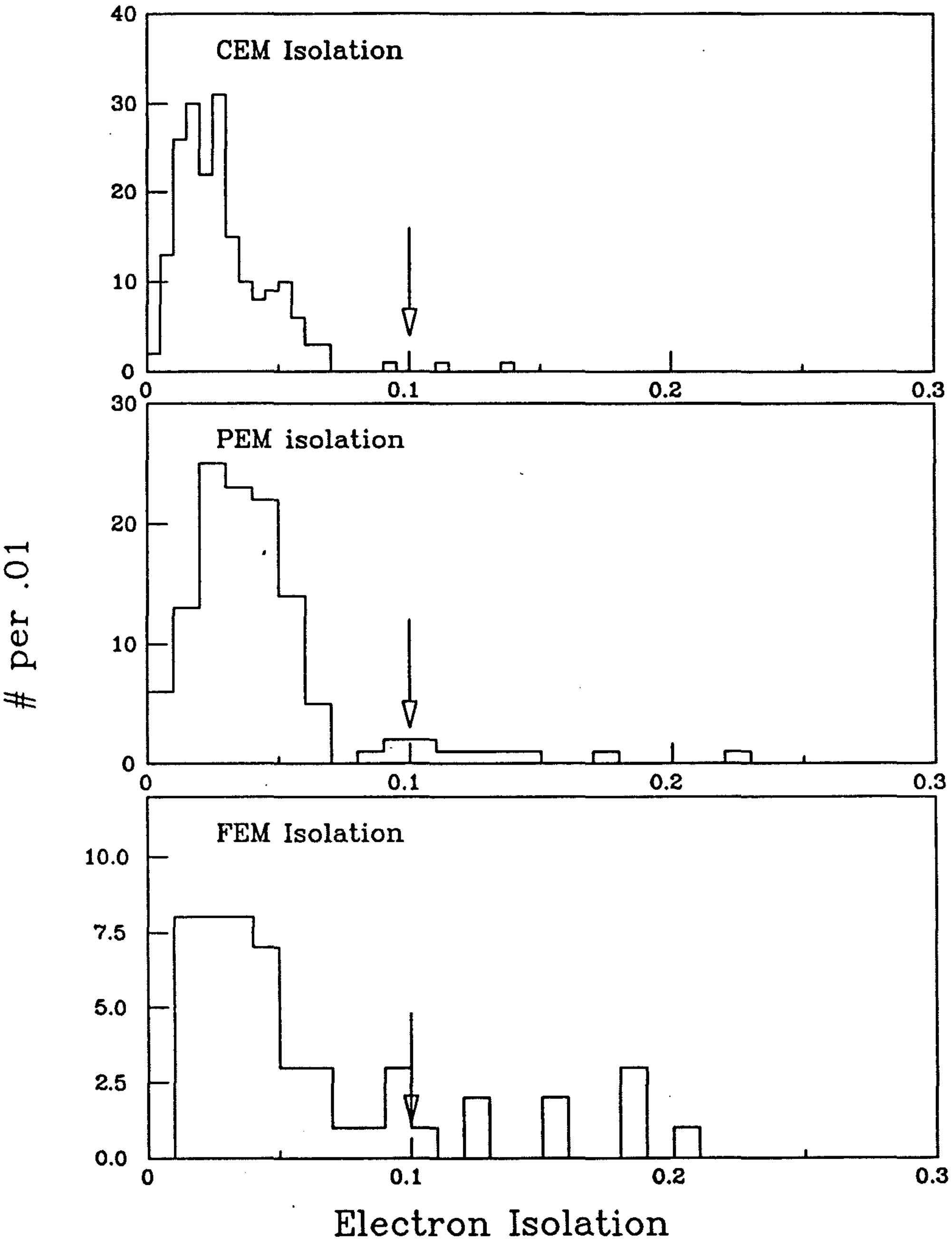

Figure 4.2: Isolation for Z electrons. The events are taken from the efficiency analysis using Z electrons.

4.4 Electron Quality Selection

For the cross section analysis, Had/EM and isolation are cuts applied to all electron candidates. There are several other variables that we use depending on which detector the electron is in:

4.4.1 Identifying a Central Region Electron

The variables listed below are used to select CEM electrons:

Had/EM	We apply a loose cut that is a function of electron energy: the cut requires Had/EM < .055 + .045/E. This maintains high efficiency for electrons of very high E_t, where the shower is more penetrating and leaks into the hadronic compartment.
E/P	This is the ratio of CTC track momentum to the corrected CEM energy.
LSHR	Measures the lateral sharing of energy in a CEM cluster. The CES z-location is used to predict the distribution of energy between the seed tower and adjacent towers. This is compared to the measured energy.
χ^2_{strip}	The shape of the CES strip cluster (the z-view) is compared to a parametrization determined from testbeam electrons.
Δx	This is the distance in cm between the extrapolated track position and the wire cluster position in the ϕ-view.
Δz	This is the distance in cm between the extrapolated track position and the strip cluster position in the z-view.

When we calculate the track-shower matches Δx and Δz, we correct for CTC-CES alignment using an ***in situ*** survey derived from 12,000 inclusive electrons. Figures 4.3- 4.4 show distributions of the CEM variables for isolated electrons. These distributions are from the studies of electron efficiency described in section 5.3.1. Figure 4.3 is taken from an unbiased sample of isolated Z^0 electrons. Figure 4.4 has the same distributions with better statistics, taken from an unbiased sample of W electrons.

4.4.2 Identifying a Plug and Forward Region Electron

In this analysis, we always require a CEM electron that satisfies strict cuts. Because of this, we only need use a few loose cuts to select gas electrons for a clean sample of C-P and C-F dielectron events. For PEM and FEM we require Had/EM < .05 and Isolation < .10. For the FEM, we make no further requirements. For the PEM, we also use the transverse shape of the shower and look for an indication of a track pointing to the shower. The variables listed below are used to select PEM electrons:

$\chi^2_{3\times 3}$	The transverse shape of the calorimeter cluster, using the 3×3 pads surrounding the seed tower, is compared to a shower parametrization determined from testbeam electrons.
VTPC Occupancy	This is a loose tracking cut that identifies the likely presence of a charged track in the VTPC. A road is determined pointing from the collision vertex to the EM cluster position. The road is from .041 to .035 radians wide in ϕ and from .125 to .022 wide in $d(\cot\theta)$, depending on the angle between the EM cluster and the beamline. The number of VTPC hits found in the road is divided by the number of VTPC wires crossed by the road. If the ratio is greater than .5 we assume a charged track is present. If the road is too close to one of the radial boards that separates the VTPC into octants, the occupancy defaults to 1.0 so that no cut is applied.

Figure 4.5 shows distributions of these variables for isolated electrons.

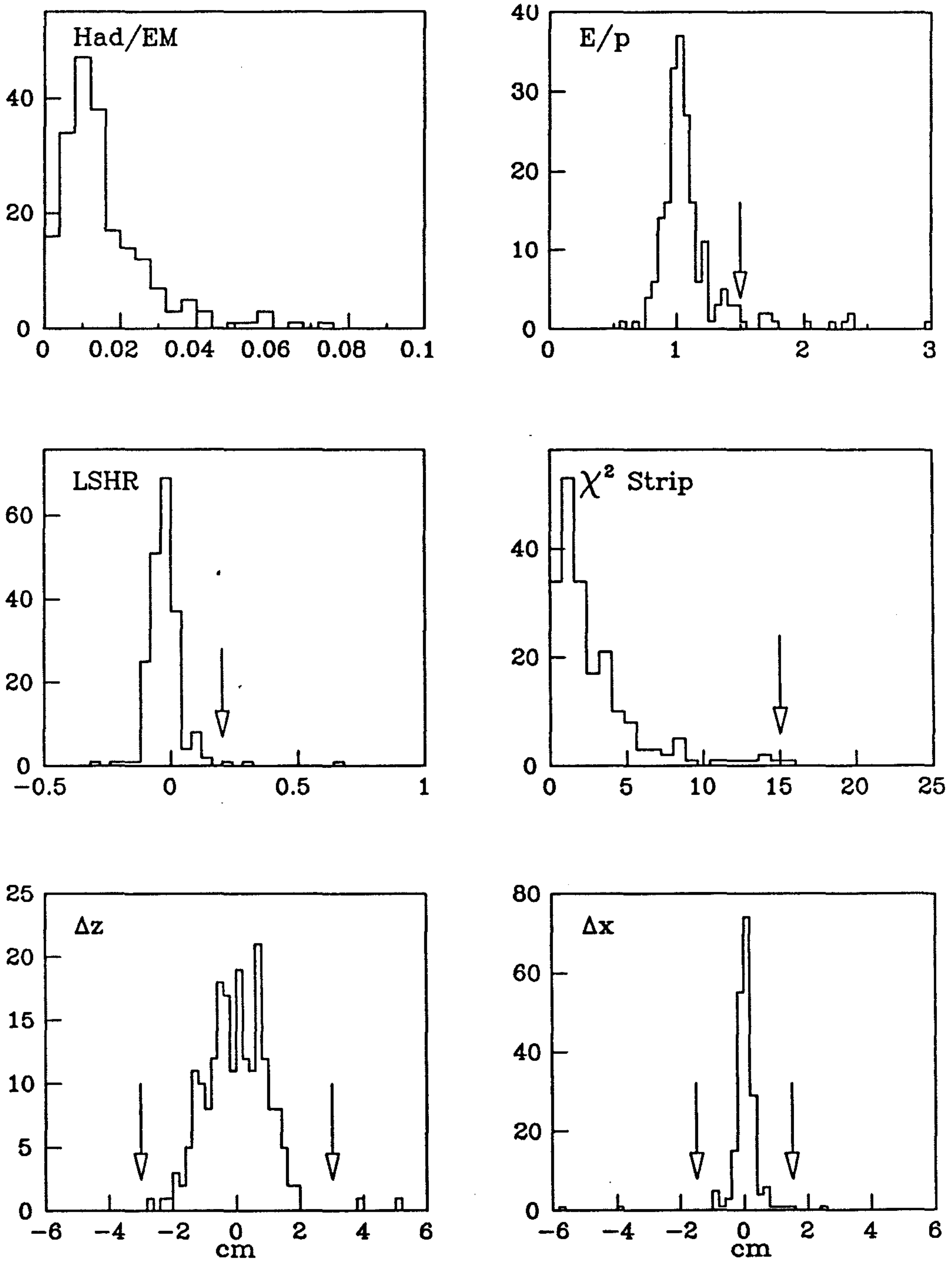

Figure 4.3: The variables used to identify CEM electrons. The distributions are taken from the efficiency analysis using Z^0 electrons. Arrows indicate the cuts used in the cross section analysis.

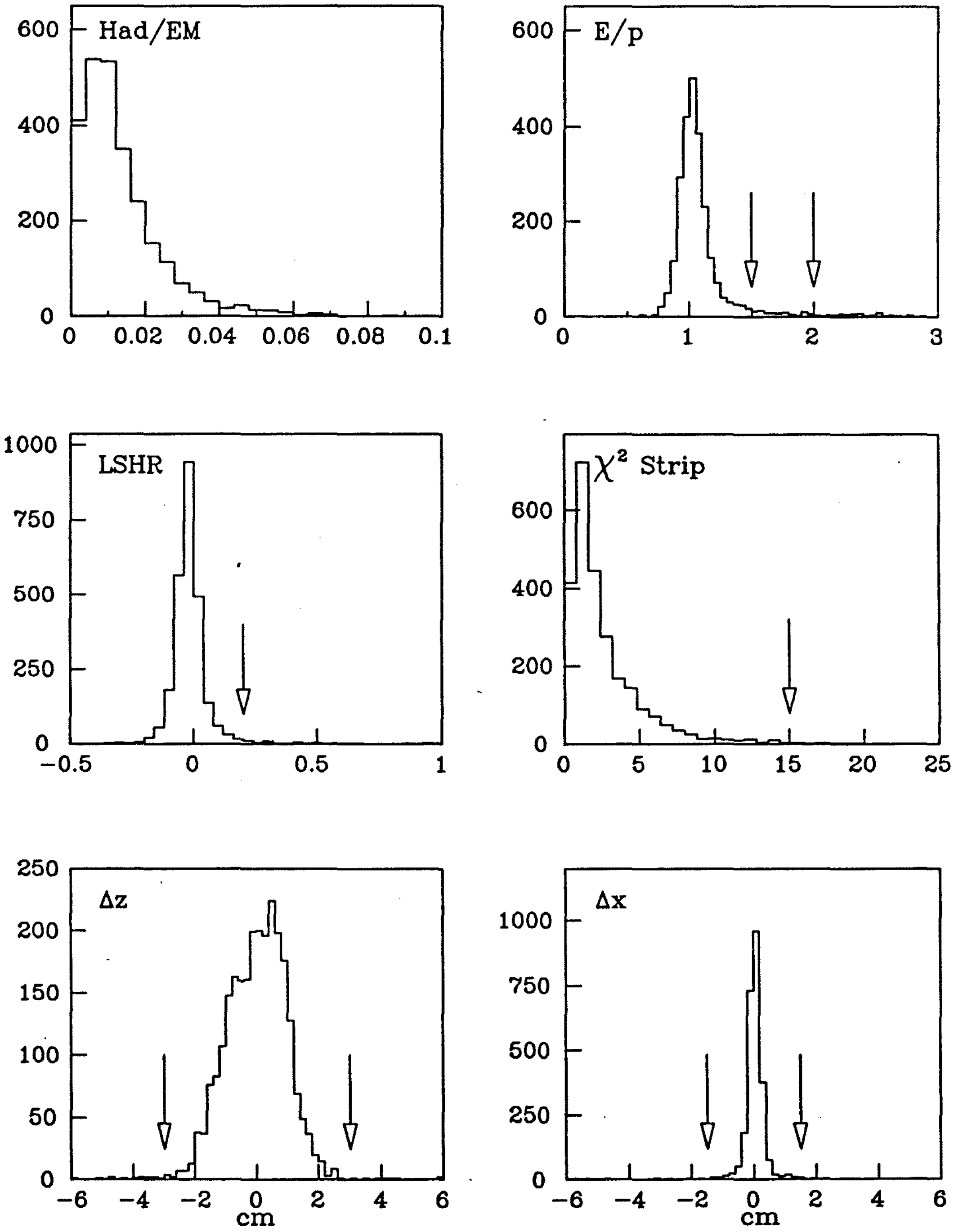

Figure 4.4: The variables used to identify CEM electrons. The distributions are taken from the efficiency analysis using W electrons. Arrows indicate the cuts used in the cross section analysis.

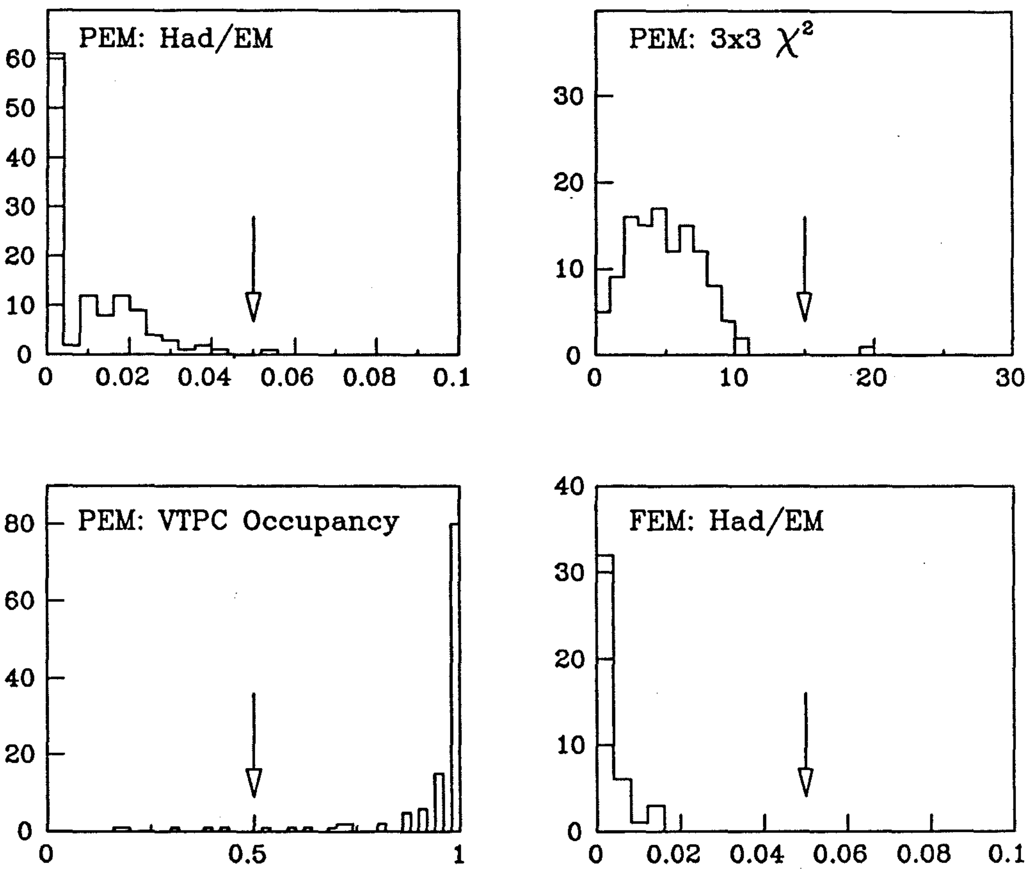

Figure 4.5: The variables used to identify PEM and FEM electrons. The distributions are taken from the efficiency analysis using Z^0 electrons.

Chapter 5

Measurement of $\sigma \cdot B(Z^0 \rightarrow e^+e^-)$

5.1 Event Selection

The cuts used to select electrons are listed in tables 5.1 and 5.2. A candidate event must contain one CEM electron with $E_t > 15$ GeV that passes the tight set of cuts. A second EM cluster with $E_t > 15$ GeV must also be present that passes the loose set of cuts. Each electron must pass fiducial cuts; these will be described in the next section. In addition, we require that the ELECTRON_12 trigger was satisfied (see p. 23). Finally, we require that the collision vertex be ±60 cm of the origin. There are 303 events that pass these cuts.

The invariant mass is calculated for the two highest E_t electrons that satisfy the electron selection cuts. The mass is calculated from the four vectors for each electron (p_x, p_y, p_z, E):

$$M^2 = (E^1 + E^2)^2 - (p_x^1 + p_x^2)^2 - (p_y^1 + p_y^2)^2 - (p_z^1 + p_z^2)^2, \tag{5.1}$$

where we neglect the small electron mass. The energy is the total corrected energy in the EM compartment of the calorimeter. The direction is our best estimate for the electron direction, as described in section 4.3.

The mass distribution for the 303 events is shown in figure 5.1. Of these, 254 events have an invariant mass between 75 and 105 GeV.

E_t	$>$	15 GeV
Iso(r=.4)	$<$	.1
E/p	$<$	1.5
LSHR	$<$	.2
χ^2_{strip}	$<$	15
$\|\Delta x\|$	$<$	1.5 cm
$\|\Delta z\|$	$<$	3.0 cm
Had/EM	$<$	$.055 + .045E/100$

Table 5.1: Tight CEM electron cuts.

E_t	$>$	15 GeV
Iso(r=.4)	$<$	.1
If CEM electron:		
E/p	$<$	2.0
If PEM electron:		
$\chi^2_{3\times3}$	$<$	20
VTPC occupancy	$>$	0.5
Had/EM	$<$	.05
If FEM electron:		
Had/EM	$<$	.05

Table 5.2: Loose second electron cuts.

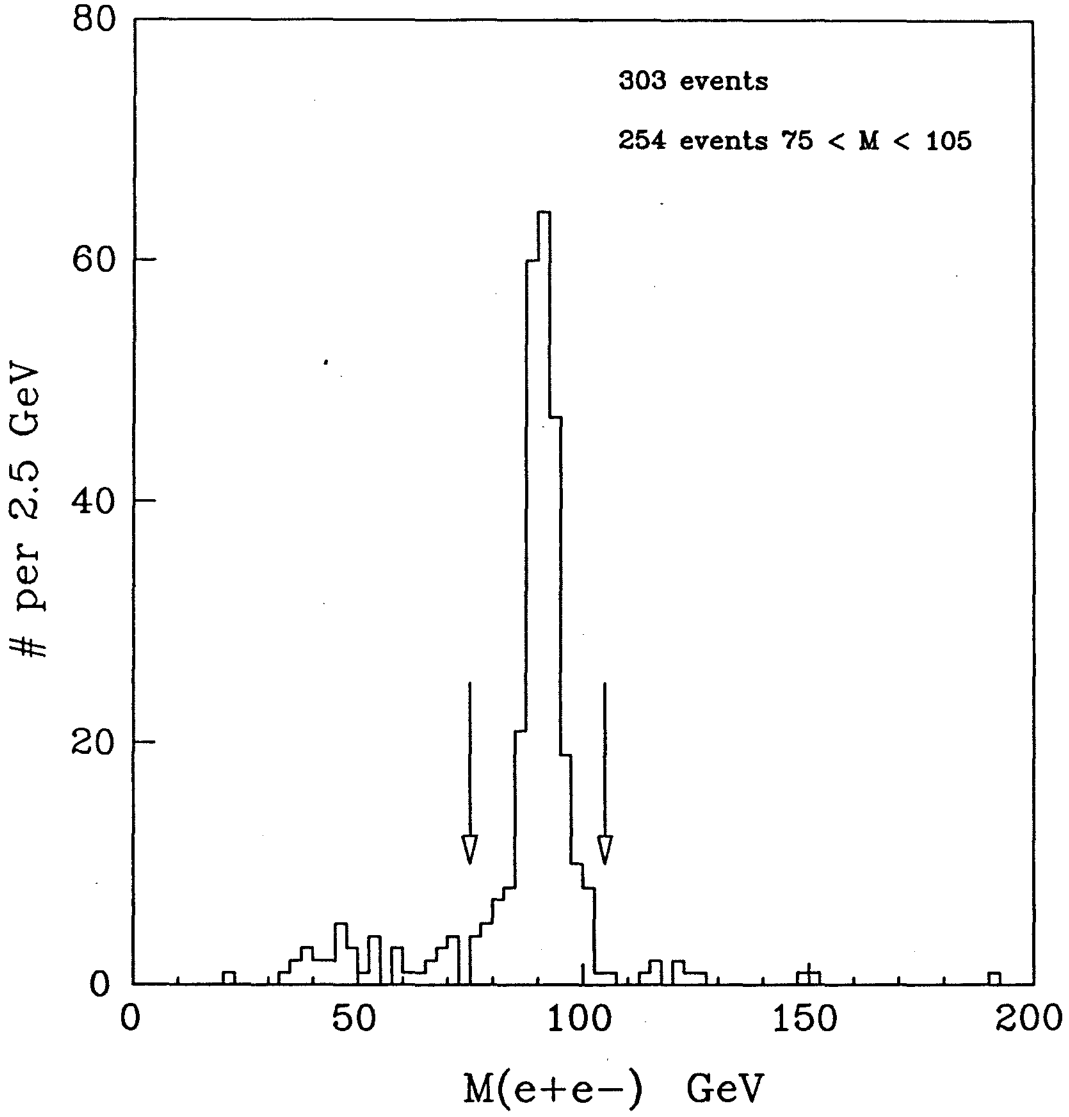

Figure 5.1: The mass distribution for events passing the dielectron event selection.

5.2 Acceptance

5.2.1 Fiducial Cuts

To accurately account for the number of events observed we restrict our electrons to well-understood regions of the detector. This is mostly a case of avoiding the cracks between detector modules. One electron is required to be in the CEM. The fiducial cuts for CEM electrons are listed below:

CEM Fiducial Requirements

- Extrapolated track ϕ-position must be ± 21 cm from tower center. Within these bounds the electron is at least 3.24 cm from the 15° wedge boundaries.
- Extrapolated track z-position must be > 9 cm from $z = 0$. This avoids the crack at 90° where the east and west arches meet.
- Seed tower of cluster must not be the outermost tower in wedge; see figure 3.1b. This tower is the most extreme case of the projective geometry and requires large energy corrections.
- Seed tower of cluster must not be the tower containing the access to the solenoid cryostat.

The second electron may be in the CEM, PEM or FEM. If it is in from the CEM, the above fiducial cuts are applied. If it is in the PEM or FEM the cuts are primarily for avoiding the quadrant edges:

PEM and FEM Fiducial Requirements

- Seed tower of cluster must not be at a ϕ-boundary.
- Seed tower of PEM cluster must not be in the two inner or two outer bands in eta.

- Seed tower of FEM cluster must not be in the small pads near the beampipe ($4.2 > |\eta| > 3.7$).
- Seed tower of PEM cluster is excluded from 16 dead PEM channels. Most of these happen to be in the quadrant boundaries already excluded.

The distribution of good fiducial regions in $\eta - \phi$ space is shown in figure 5.2.

5.2.2 Simple Detector Model

We estimate the acceptance using particle 4-vectors from the ISAJET Monte Carlo event generator [28]. An outline of the calculation is as follows:

1. Generate N_{gen} Z^0 events; the mass distribution is a Breit-Wigner with the Standard Model width.
2. Generate a z-vertex position from a gaussian with mean = 0 and $\sigma = 30$ cm. This is based on the z-vertex distribution of the data.
3. Extrapolate the electron vectors to the calorimeter.
4. Make fiducial cuts on the extrapolated position consistent with the cuts made on the data. We keep only C-C, C-P and C-F topologies.
5. Smear the electron energy by the calorimeter resolution, including a constant term that estimates the tower-to-tower variation in response:

$$\begin{array}{rrrcr} \text{CEM:} & (\sigma_E/E)^2 = & (.135/\sqrt{E_t})^2 & + & (.017)^2 \\ \text{PEM and FEM:} & (\sigma_E/E)^2 = & (.28/\sqrt{E})^2 & + & (.02)^2 \end{array}$$

6. Make the $E_t > 15$ GeV cut on each electron.
7. Calculate the invariant mass using the smeared energy.
8. For each topology C-C, C-P and C-F, count n_{cc}, n_{cp} and n_{cf} events with smeared mass in the range from 75-105 GeV.

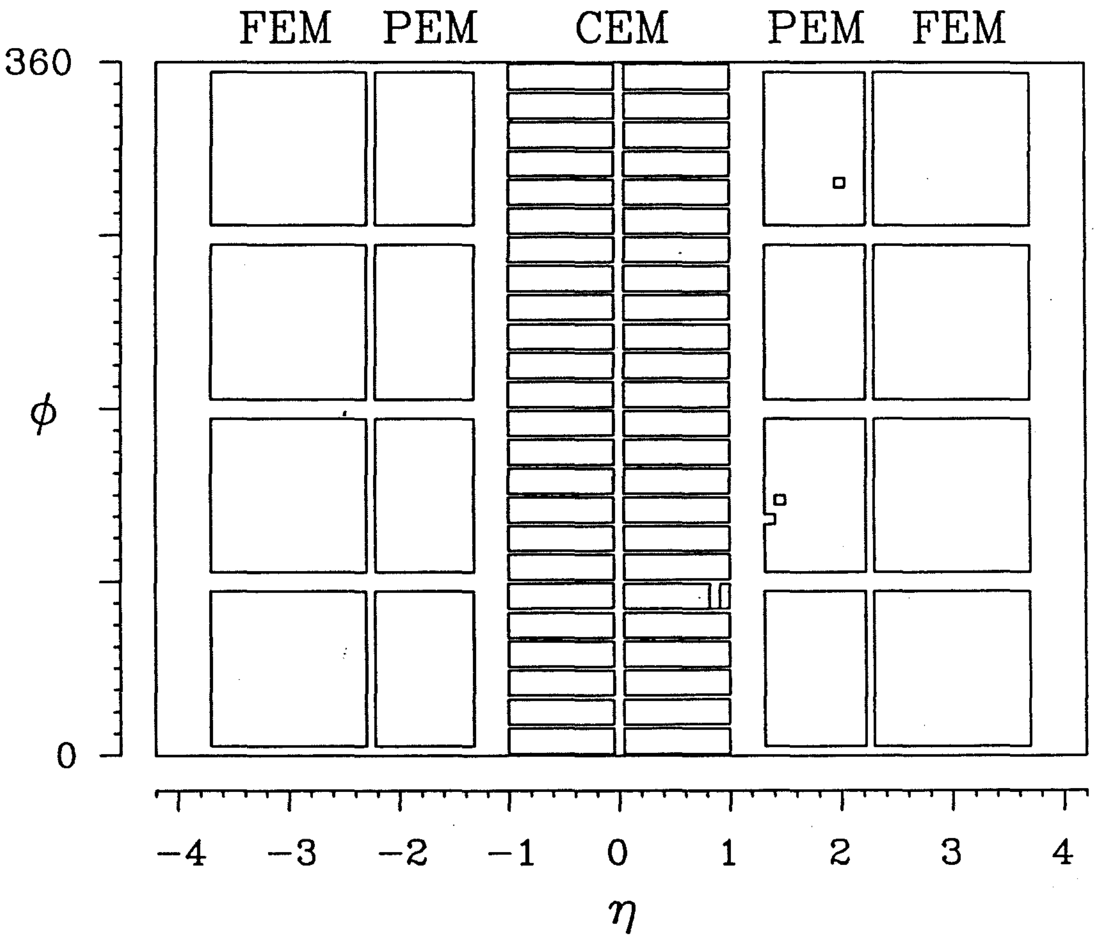

Figure 5.2: The fiducial volume for good electrons. The solenoid cryostat access is responsible for the gap at 90 degrees in the CEM. The three dead PEM towers away from the quadrant edges are also indicated.

9. Using EHLQ-1 parton distributions [29] in the ISAJET generation, we obtain the following acceptances for each topology:

Monte Carlo Acceptance			
$a_{cc} \equiv$	n_{cc}/N_{gen}	$=$	$.139 \pm .002$
$a_{cp} \equiv$	n_{cp}/N_{gen}	$=$	$.166 \pm .002$
$a_{cf} \equiv$	n_{cf}/N_{gen}	$=$	$.058 \pm .001$

Note that this definition of acceptance includes the correction due to the finite width of the Z^0. Whereas the theoretical calculation of the cross section is based on a δ-function, we observe a Breit-Wigner broadened by the resolution of the calorimeters. Since we generate a mass distribution based on a Breit-Wigner, and smear the reconstructed mass, we are accounting for the fraction of events that fall outside of the mass window. We have varied the resolution coeeficients by ±1% and see no change in the acceptance. This is because the mass resolution is good enough ($\simeq 1.5$ GeV) that the Breit-Wigner is well contained in the 30 GeV mass window.

5.2.3 Choice of structure function

The acceptance we measure depends on the choice of structure function used in generating the Z^0 events. This is because the structure functions have different distributions for the parton momentum fraction. This affects the longitudinal boost of the Z^0 which affects the proportion of C-C, C-P and C-F events. For our final results we use the EHLQ-1 structure functions. We estimate the contribution to the uncertainty in our final result using a variety of structure functions. Because a_{cc}, a_{cp} and a_{cf} are correlated, we carry out the cross section measurement using each result and use the maximum variation in $\sigma \cdot B$ (1.5%, or 3 pb) as the systematic error. Table 5.3 lists the results of this study.

5.2.4 Checks on the Acceptance Calculation

Our acceptance model is based on the premise that we are generating events with nearly the same kinematics as the Z^0 events that we produce in $\bar{p}p$ collisions. We check this by comparing several distributions from the Monte Carlo sample with the same distributions from our final sample of Z^0 candidates. For the Monte Carlo sample we begin with the

Structure function		a_{cc}	a_{cp}	a_{cf}	a_{tot}	$\Delta\sigma \cdot \mathrm{B}$
EHLQ1	[29]	.139	.166	.058	.363	nominal
EHLQ2	[29]	.139	.169	.058	.366	−1.0%
DO1	[30]	.138	.162	.060	.360	+0.5%
DO2	[30]	.139	.165	.063	.367	−1.0%
MRSE	[31]	.140	.166	.057	.363	0.0%
MRSB	[31]	.142	.168	.056	.366	−1.0%
HMRSE	[32]	.140	.165	.056	.361	+0.5%
HMRSB	[32]	.142	.168	.056	.366	−1.0%
DFLM1	[17]	.136	.165	.056	.357	+1.5%
DFLM2	[17]	.140	.167	.058	.365	−0.5%
DFLM3	[17]	.140	.166	.057	.363	0.0%

Table 5.3: Variation in acceptance due to choice of structure function.

events that passed the above simple detector model. The selection and isolation efficiency for the electron cuts has been measured from the data (section 5.3); from this we calculate event efficiencies of .85, .79 and .84 for C-C, C-P and C-F topologies respectively. For each event we throw a uniform random number between 0.0 and 1.0 and discard it if the random number exceeds the efficiency for that topology. We then compare distributions of the surviving Monte Carlo events with distributions of our final sample of Z^0 candidates, and find good agreement, as discussed below.

The kinematics of an event can be factored into the longitudinal and transverse motion of the Z^0. Figures 5.3 and 5.4 compare p_t^Z and p_l^Z for the Monte Carlo sample and the data, showing reasonable agreement. Figure 5.5 compares the smeared Monte Carlo mass distribution with the data. This confirms that the energy resolution is adequately modeled.

We also compare the detector occupancy of the electrons. Figure 5.6 shows the distribution of the eta tower index for each electron in the event. The gaps in eta are from the fiducial cuts at the edges of the detectors. The dip in the middle of the central region due to the 90° crack. Finally, we compare the observed fraction of C-C, C-P and C-F events:

Data				Monte Carlo
C-C:	$n_{cc} =$	103	$f_{cc} = .406 \pm .031$	$.387 \pm .004$
C-P:	$n_{cp} =$	111	$f_{cp} = .437 \pm .031$	$.447 \pm .004$
C-F:	$n_{cf} =$	40	$f_{cf} = .157 \pm .023$	$.167 \pm .003$

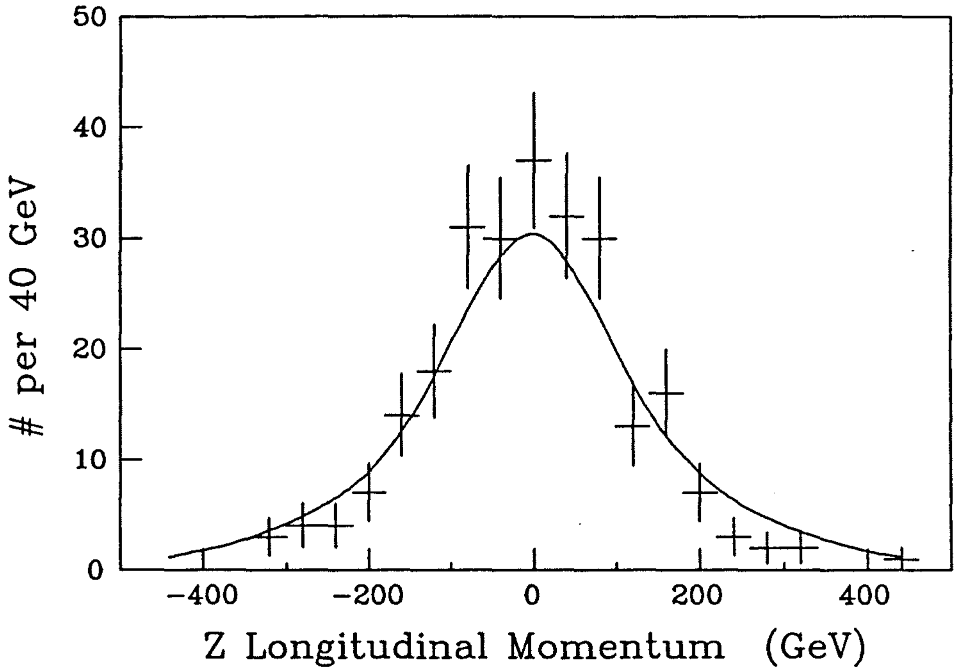

Figure 5.3: Comparison of p_l^Z for Monte Carlo (curve) and data (plotted points).

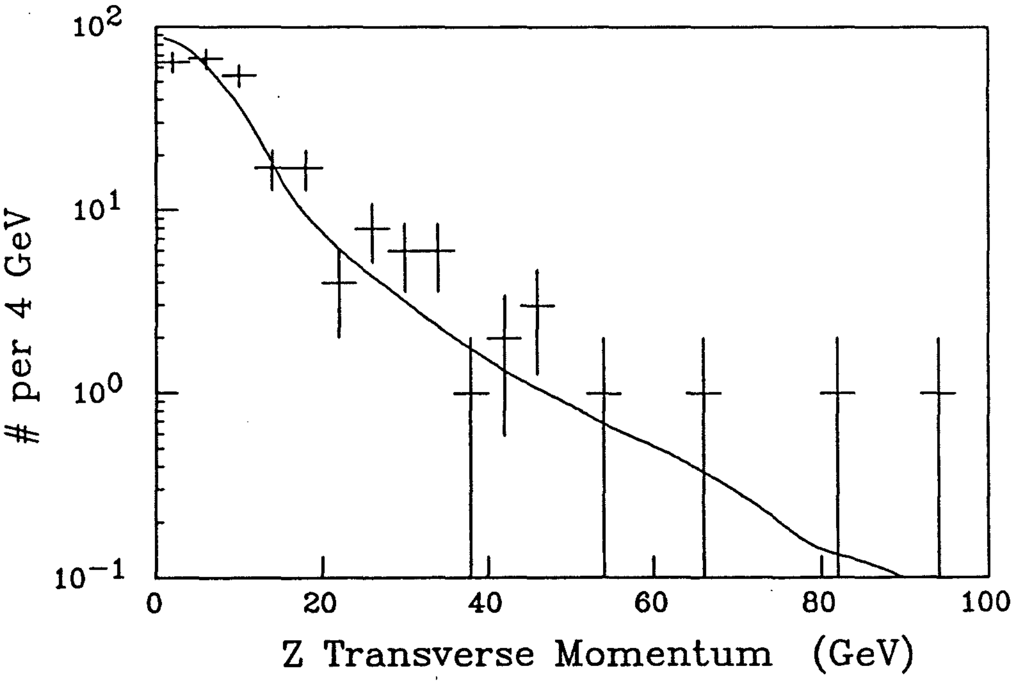

Figure 5.4: Comparison of p_t^Z for Monte Carlo (curve) and data (plotted points).

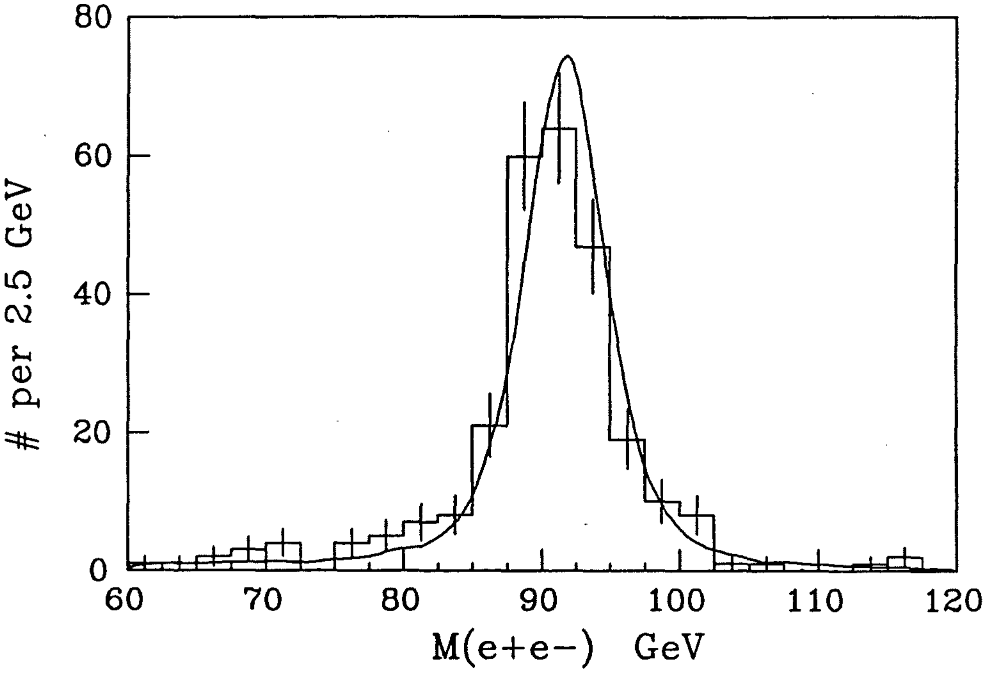

Figure 5.5: Comparison of mass distribution for Monte Carlo (curve) and data (plotted points).

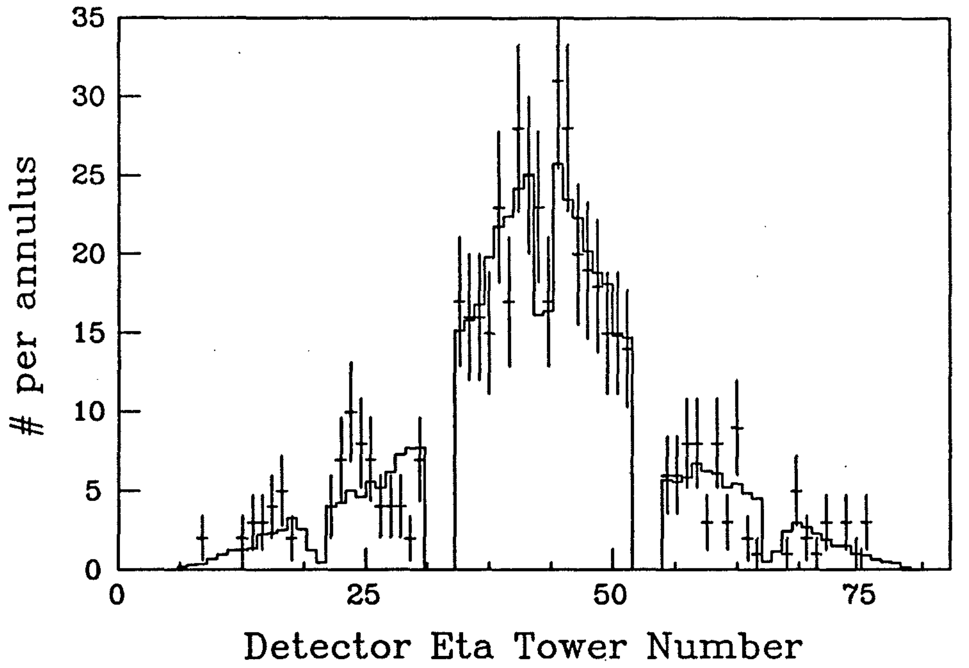

Figure 5.6: Comparison of electron tower occupancy for Monte Carlo (histogram) and data (plotted points).

5.2.5 Acceptance for Hard Wide-Angle Bremsstrahlung

A final small effect that we include in our acceptance estimate is the loss of events that radiate a hard photon and fall out of the mass window. This process is shown in figure 5.7. In this process, the 3-body final state will reconstruct to the mass of the Z^0, but the dielectron mass will be somewhat smaller. In some cases the mass falls out of the 75 to 105 GeV window. The ISAJET Monte Carlo used in the previous section does not include this effect; we apply a factor estimated separately.

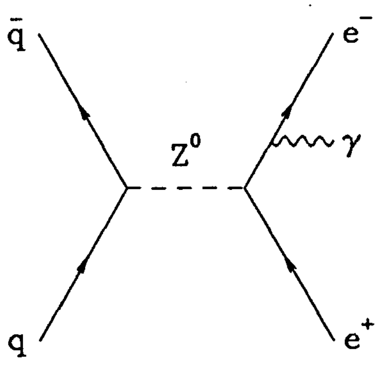

Figure 5.7: Diagram for the radiative decay $Z^0 \rightarrow ee\gamma$.

We use the same radiative Monte Carlo generator used in the CDF Z^0 mass publication [23], [33]. The Monte Carlo is based on the QED corrections to W and Z^0 decay published by Berends and Kleiss [34]. As in the previous section, we use a simple detector model. We generate a large sample of events, extrapolate the electrons to the detector and make kinematic and fiducial cuts. For each event we calculate the 3-body and dielectron invariant mass. We find that a total of 5.2% of the events that should be accepted in the mass window fall outside when we only calculate the dielectron mass.

This is a crude overestimate, because the photon is usually emitted collinear to the electron and the photon energy is detected overlapping the electron shower. To improve our estimate we plot the acceptance as a function of α, the 3-dimensional opening angle between the photon and the nearest electron. The acceptance is calculated assuming all of the low-mass events with $\alpha < \alpha_{crit}$ actually pass the mass cut and all low-mass events with $\alpha > \alpha_{crit}$ actually fail. This is plotted in figure 5.8.

To arrive at a reasonable estimate for this effect, we consider the angles pertinent to the calorimetry segmentation. A single CEM tower is .26 radians in ϕ by .1 units in η; gas towers are .09 radians in ϕ by .1 units in η. If the photon goes into the same tower as the electron, the mass calculated from two EM clusters will be a good measurement of the actual mass. This gives a solid lower limit on the acceptance of .987. A more realistic lower limit of .990 comes from including a photon that is within a radius of .2 of the electron shower; this is roughly the cluster size limit of the offline EM clustering algorithm. A solid upper limit of .994 comes from a radius of .4: this is well outside the clustering limit, and is the cone used to calculate isolation. Considering these effective critical angles, we estimate the acceptance from this effect to be $a_{ee\gamma} = .992 \pm .005$.

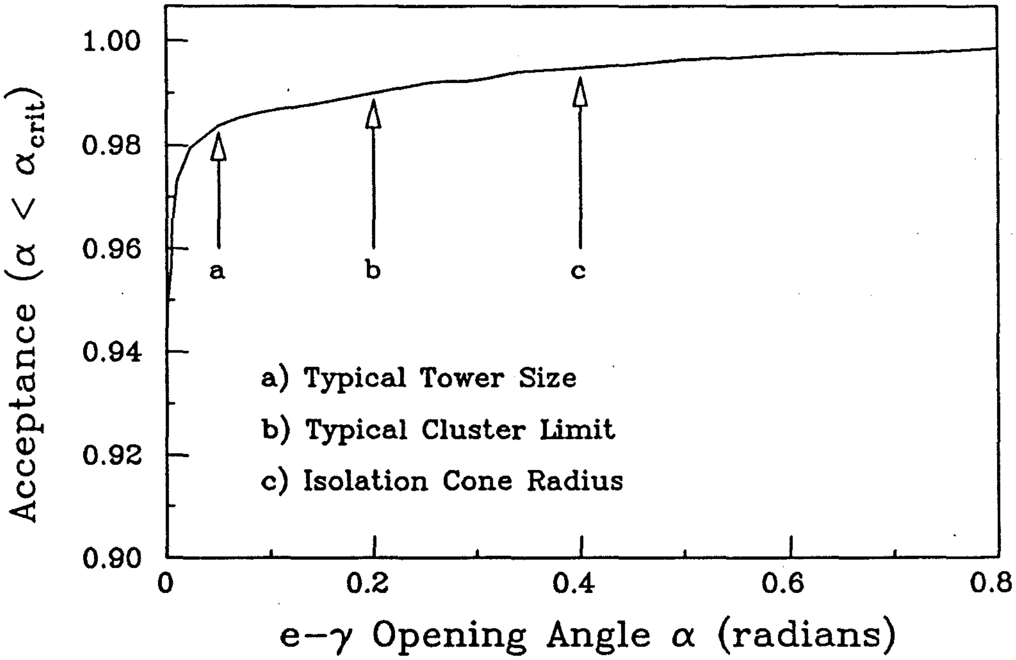

Figure 5.8: Mass window acceptance for $Z^0 \to ee\gamma$ events where the photon must be within angle α of the electron for the mass to be undiminished.

5.3 Efficiency

We measure the efficiency for the cuts listed in section 5.1 using unbiased electrons selected from the CDF data sample. We employ two sources of electrons: 1) the second electron of Z candidates selected by requiring tight cuts on one CEM leg and 2) electrons from W events selected using missing E_t ($\not\!E_t$). In each case, we impose an isolation requirement on the electron to reduce non-electron background. Therefore, the selection efficiencies we calculate are actually conditional probabilities for isolated electrons. We calculate the isolation efficiency separately so that the overall efficiency is just the product of the selection efficiency and the isolation efficiency.

5.3.1 Electron efficiency estimated from Z^0 events

We calculate the selection efficiency using the second electron of Z^0 candidates as a sample of unbiased electrons. We start with events with the final electron cuts including isolation applied to one electron and a 15 GeV Et threshold applied to both electrons. The mass distributions at this step are shown in figure 5.9. To reduce the background we apply an isolation cut of .1 to the second electron, which removes events as indicated in by the dark histogram in figure 5.9. If both electrons of a C-C event passes the tight set of electron cuts we include the both electrons in our sample. We then take the events in the mass range 75-105 GeV and apply the final set of electron cuts to the isolated second electrons. The efficiency is the ratio of the number of electrons that pass all cuts to the number of electrons considered:

Electron Efficiency estimated from Z^0 events

$$\epsilon \equiv \frac{N(e \text{ passing cuts})}{N(\text{isolated } e \text{ candidate})}$$

CEM tight cuts:	ϵ_{c1}	=	179/205	=	.873 ± .023
CEM loose cuts:	ϵ_{c2}	=	193/205	=	.941 ± .016
PEM loose cuts:	ϵ_p	=	111/118	=	.941 ± .022
FEM loose cuts:	ϵ_f	=	40/40	=	1.000 ± .025

Note that even without the isolation cut, there is very little background evident in figure 5.9. Using the same the background estimation techniques described in section 5.4 we estimate a background from QCD of 2 events for C-C, 4 events for C-P and 3 events for C-F. The presence of background might cause us to underestimate our efficiency depending on how probable it is that the fake electron will fail the quality cuts. We estimate a pessimistic systematic uncertainty by subtracting these background estimates from the efficiency denominators. The biggest change is $\epsilon_p \rightarrow 111/114 = .973$, a change of only 1.5σ of the statistical uncertainty. We conclude that the total uncertainty of these estimates is approximately that determined by the statistics of the sample.

The distributions for each of the cut variables are shown in figures 4.3 and 4.5 in section 4.4. These represent electrons in the CDF environment, biased only by requirements of isolation and $E_t > 15$ GeV. They are appropriate distributions for tuning the full detector simulation.

5.3.2 Electron efficiency estimated from W events

We also measure the CEM selection efficiencies using W events. The W event selection begins with a loose electron selection that requires a CEM cluster with $E_t > 25$ GeV and a track pointing at the cluster with $p_t > 7.5$ GeV. To select W events we require $\not{E}_t > 20$ GeV and also cut on the the significance of the measurement:

$$\sigma_{\not{E}_t} \equiv \frac{\not{E}_t}{\sqrt{\sum\limits_{towers} E_t}} > 2.5. \tag{5.2}$$

The largest remaining background is dijet events with one poorly measured jet opposite a jet faking an electron. To reject these events we look at a slice of calorimeter 180° ± 30° away from the ϕ location of the electron candidate. If there is a jet cluster with $E_t > 10$ GeV in this region we exclude the event. Finally, we calculate the transverse mass of the W candidate, defined as:

$$M_t \equiv \sqrt{2E_t\not{E}_t(1 - \cos(\phi_e - \phi_{\not{E}_t}))}. \tag{5.3}$$

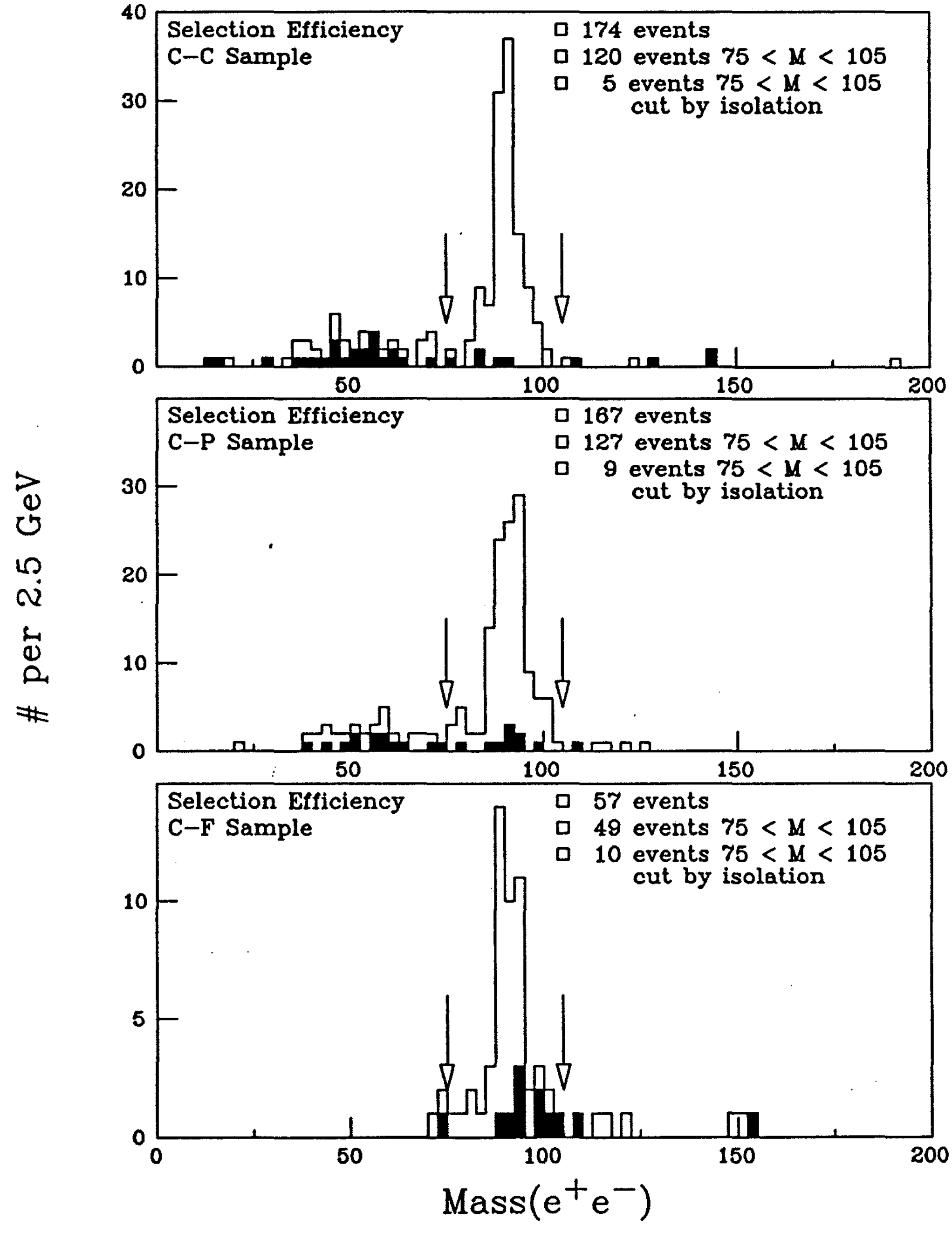

Figure 5.9: Mass distributions for the samples used to estimate electron selection efficiency. The large histogram contains the events that have one good isolated CEM electron present. The dark histogram contains the events that are removed by requiring that the second electron be isolated.

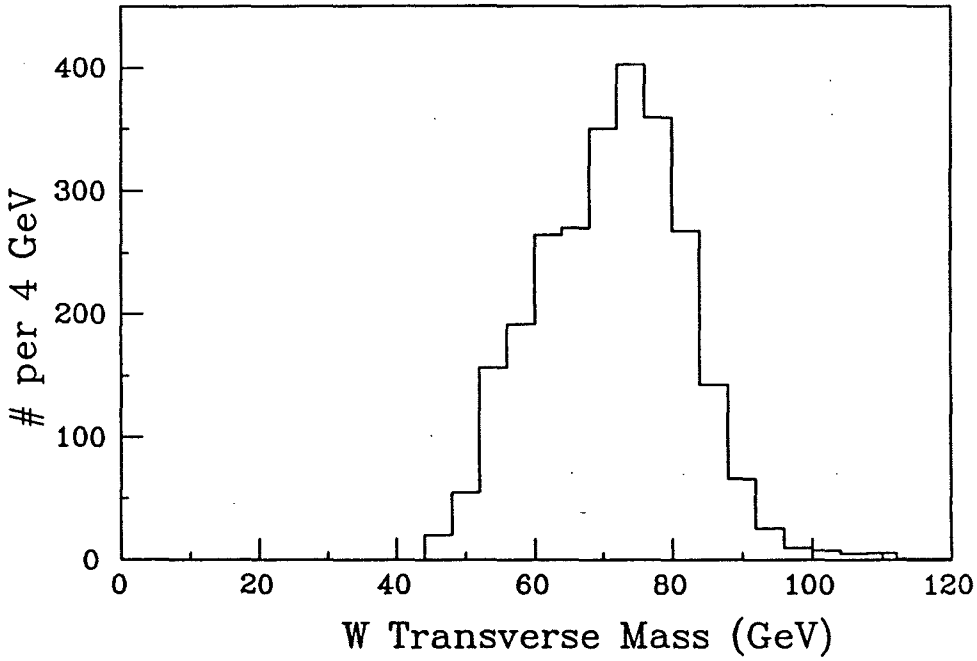

Figure 5.10: The transverse mass distribution for the events used to estimate the electron efficiency

The transverse mass distribution is a characteristic signature for W production; in figure 5.10 this is plotted for the events used to calculate the electron efficiency. We then apply the standard isolation cut of .1 to the candidate electrons. We see how many of those passing this cut also pass the tight CEM electron cuts. We use the same procedure to find the efficiency for the loose CEM electron cuts ($E/p < 2$). Both results are tabulated below:

CEM Electron efficiency from W events	
$\epsilon_{c1} = \frac{2331}{2698} =$	$.864 \pm .007$
$\epsilon_{c2} = \frac{2554}{2698} =$	$.947 \pm .004$

These efficiencies are correct if we have formed an electron sample with negligible background. If we had not first required isolation, the above method would give a tight cut efficiency of .825; this is lower because jets faking electrons are particularly likely to fail one or more of these cuts.

The distributions for each of the variables are shown in figure 4.4 in section 4.4.

We summarize below the contribution to the total efficiency from each of the cut variables. We have found that most of them are uncorrelated; the exception being E/p and Δx. Because of the correlations, the product of the individual efficiencies is somewhat less than the efficiency for all of the cuts applied together. The efficiencies calculated using W electrons agrees well with the results from the second Z^0 electron.

Cut Variable	ϵ from 2nd Z^0 electrons	ϵ from W electrons
all tight CEM cuts	$.873 \pm .023$	$.875 \pm .007$
Had/EM $< .055 + .045E$	$1.000 \pm .005$	$.998 \pm .001$
$E/p < 1.5$	$.912 \pm .020$	$.916 \pm .005$
LSHR $< .2$	$.985 \pm .008$	$.975 \pm .003$
$\chi^2_{\text{strip}} < 15$	$.976 \pm .011$	$.974 \pm .003$
$\|\Delta z\| < 3$ cm	$.985 \pm .008$	$.979 \pm .003$
$\|\Delta x\| < 1.5$ cm	$.963 \pm .004$	$.966 \pm .013$
loose CEM: $E/p < 2.0$	$.941 \pm .016$	$.950 \pm .004$
all PEM cuts	$.941 \pm .022$	–
Had/EM $< .05$	$.992 \pm .008$	–
$\chi^2_{3\times3} < 15$	$.992 \pm .008$	–
VTPC occupancy $< .5$	$.958 \pm .019$	–
FEM cut: Had/EM $< .05$	$1.000 \pm .005$	–

5.3.3 Isolation efficiency

The isolation efficiency was estimated assuming azimuthal symmetry for the Z^0 decay. The isolation is recalculated assuming the electron might have hit other locations in the detector, at the same η as the original electron but at a different value of ϕ. For each electron in each event, an equivalent isolation can be calculated several times.

The isolation for the electron is defined as (recall equation 4.1):

$$\text{Iso}(\text{r} = .4) = \frac{\left(\sum\limits_{\text{towers}}^{\text{cone}} E_t\right) - E_t^e}{\sum\limits_{\text{towers}}^{\text{cone}} E_t}, \tag{5.4}$$

where the cone is centered on the electron position (η, ϕ). We break the sum up into two contributions, the towers in the electron cluster and the towers surrounding the electron cluster:

$$\sum_{\text{towers}}^{\text{cone}} E_t = \sum_{\text{towers}}^{\text{electron}} E_t + \sum_{\text{towers}}^{\text{surrounding}} E_t. \tag{5.5}$$

To estimate the efficiency, we calculate the isolation in a new cone centered on the same η but at a new ϕ. We calculate the equivalent sum over E_t in the new cone as follows: we sum over the towers in the new cone, but if the tower maps into a tower that was in the electron cluster, we use the tower E_t from the electron cluster. This is shown in the following equation:

$$\sum_{\text{towers}}^{\substack{\text{new}\\\text{cone}}} E_t = \sum_{\text{towers}}^{\substack{\text{original}\\\text{electron}}} E_t + \sum_{\text{towers}}^{\substack{\text{new}\\\text{surrounding}}} E_t. \tag{5.6}$$

For the CEM, ϕ locations are selected to be offset by $60°, 120°, 240°$ and $300°$ (4, 8, 16 and 20 towers) from the seed tower of the electron. This prevents the cones of radius .4 from overlapping. The cone offset by 180° (12 towers) is not used because a 2nd CEM electron often appears opposite the first. In the gas calorimeters, the ϕ locations are offset by $55°, 110°, 165°, 220°$ and $275°$ $(11, 22, 33, 44$ and 55 towers). See figure 5.11 for a graphic description of this method.

The isolation efficiencies are extracted from figure 5.12. The distributions are the equivalent isolation for a Z^0 electrons measured from the energy in cones at other ϕ locations. The efficiencies for each detector are tabulated below:

Efficiency for Electron Isolation Cuts		
$\epsilon_{\text{iso}}(\text{CEM}) \equiv$	$i_c =$	$0.985 \pm .010$
$\epsilon_{\text{iso}}(\text{PEM}) \equiv$	$i_p =$	$0.976 \pm .010$
$\epsilon_{\text{iso}}(\text{FEM}) \equiv$	$i_f =$	$0.977 \pm .020$

We have checked the CEM isolation efficiency using the complement of the technique used to find the electron selection efficiency. Here we make LSHR, E/p, χ^2_{stp}, Δz, Δx cuts on the W and Z^0 electrons and find the fraction of events that pass the isolation cuts. Had/EM is not made because we have observed a slight correlation between Had/EM and isolation. The isolation efficiency calculated from W's is $.977 \pm .003$ and from Z's is $.977 \pm .011$, in

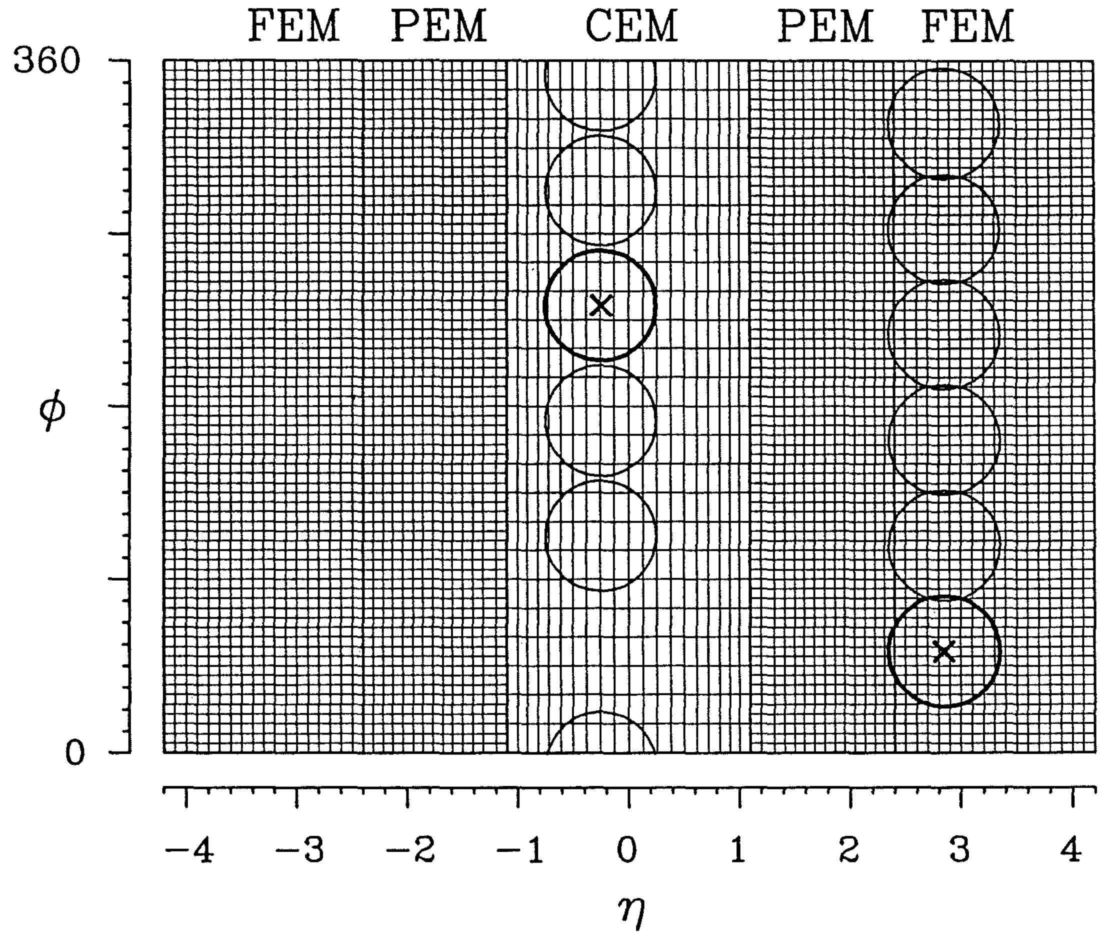

Figure 5.11: Finding the isolation efficiency using the underlying event away from the electron. The boldface ×'s mark location of the Z^0 electrons in $\eta - \phi$ space. The circles represent cones of radius .4 use to calculate isolation.

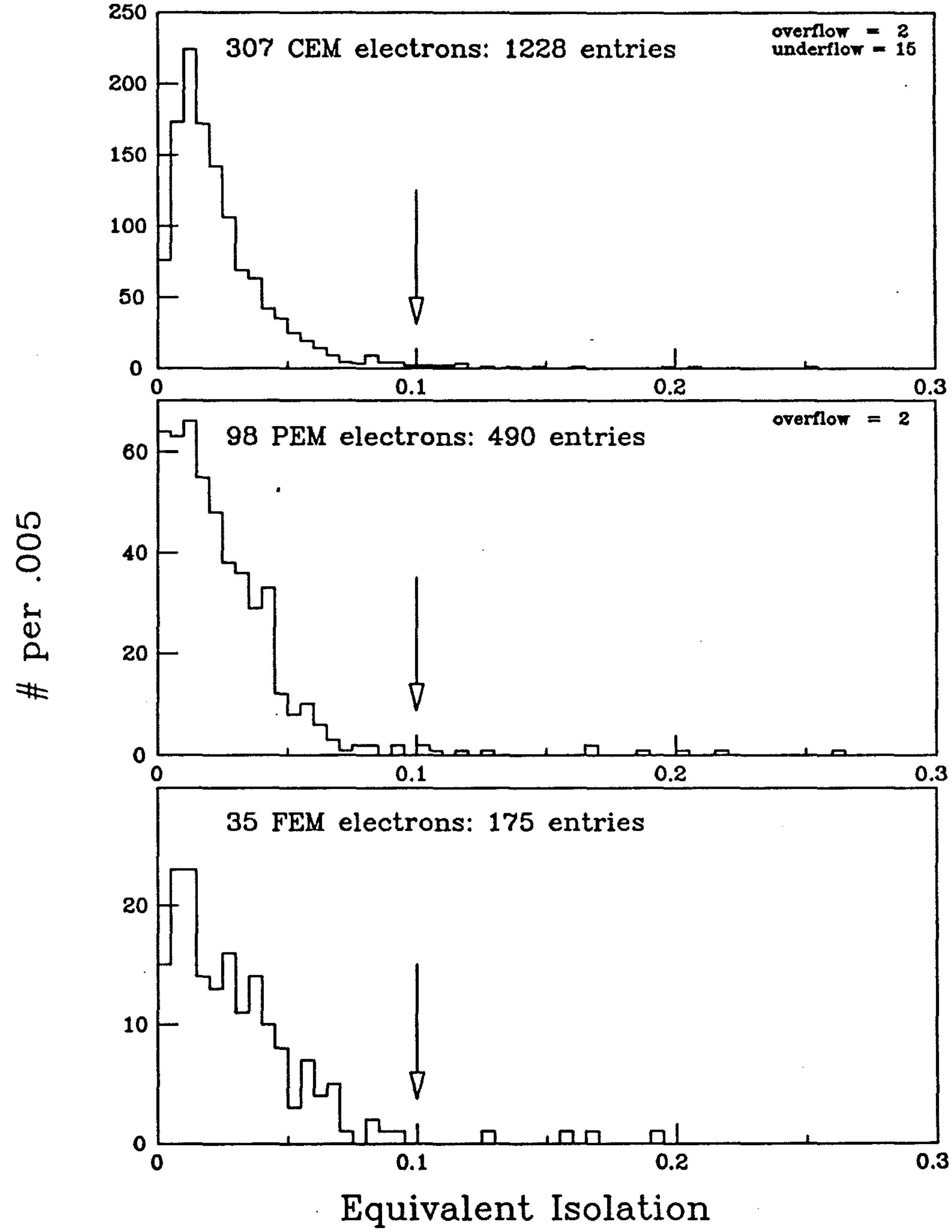

Figure 5.12: Isolation distributions calculated using underlying event away from electron.

agreement with the above method. The isolation distributions for Z^0 electrons are plotted in figure 4.2.

5.3.4 Event vertex efficiency

Because of the finite length of the Tevatron bunches, the $\bar{p}p$ collision can have a z-position many centimeters away from the origin. The distribution of collision vertices (z_v) is gaussian with a mean of 0 and σ of 30 cm. Events with large values of $|z_v|$ may have a large discrepancy between the actual E_t^e and the E_t calculated by the trigger. This is because the trigger system does not have enough time to determine a value for z_v and must use $z_v = 0$. Also, if the event vertex is very far from the origin, a particle can enter the PEM at extreme angles of incidence, or even exit the plug hole without encountering the PEM or FEM. We cut events at 60 cm or 2σ to keep the electrons in a well understood region. The efficiency for this cut is $\epsilon_{zv} = .959 \pm .005$. The uncertainty corresponds to a change in σ of 1 cm.

5.3.5 Trigger efficiency

Since we require the ELECTRON_12 trigger for our final event sample, we must account for the efficiency of this trigger. Because we run with many redundant triggers, we have event samples that we can use to measure this efficiency.

We measure the E_t threshold response of the ELECTRON_12 trigger using events that pass a pre-scaled 7 GeV trigger (n_7) and counting how many have the 12 GeV trigger satisfied (n_{12}) [37]. This ratio n_7/n_{12} is plotted in figure 5.13 versus cluster E_t. The integrated efficiency above 15 GeV is 98.4%.

For the purpose of calculating a cross section, we need the conditional probability for satisfying the trigger given that an isolated electron passes the tight and CEM cuts. We measure this using W events that pass $E_t > 15$, $\not{E}_t > 20$, $\sigma_{\not{E}_t} > 2.5$, a dijet cut as in section 5.3.2 and $M_t > 50$ GeV. We apply the tight (and loose) CEM cuts and count how many of the remaining events have the ELECTRON_12 trigger satisfied. This efficiency is

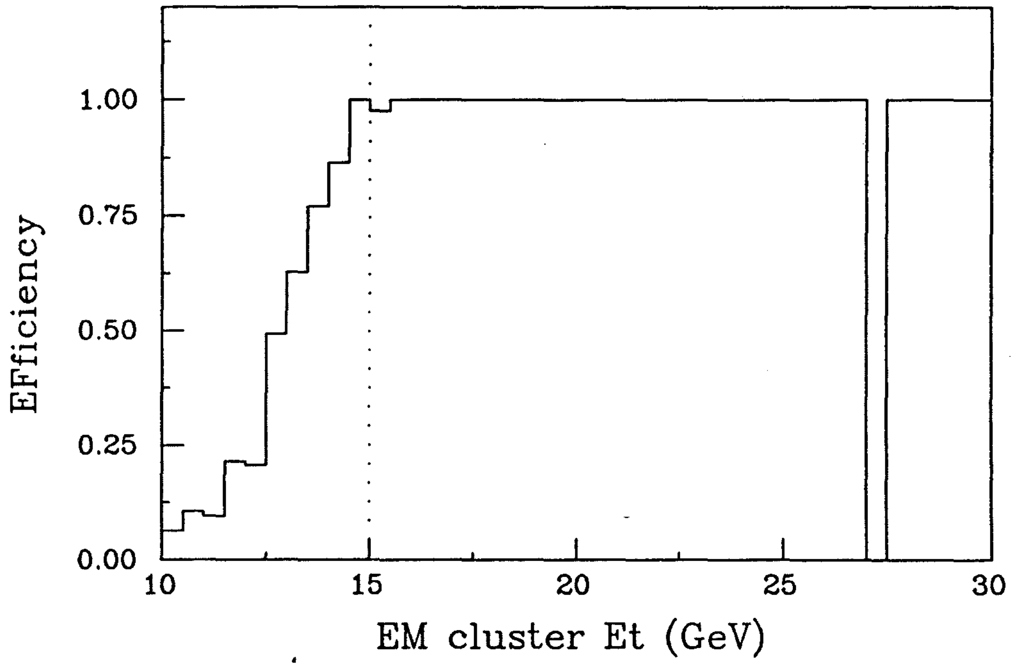

Figure 5.13: The E_t response of the 12 GeV electron trigger.

$\epsilon(trg \mid c1) = .972 \pm .004$ for the tight CEM cuts and $\epsilon(trg \mid c2) = .969 \pm .004$ for the loose CEM cuts.

For C-P and C-F events the trigger efficiency is just $t_{cp} = t_{cf} = \epsilon(trg \mid c1)$. However, a C-C Z^0 has two chances to satisfy this trigger; the trigger efficiency for these events is one minus the probability that both electrons fail the trigger :

$$t_{cc} \;=\; 1 - (1 - \epsilon(trg \mid c1))(1 - \epsilon(trg \mid c1)) \;=\; .999 \pm .001. \qquad (5.7)$$

Here we assume that the failure mode for two good CEM electrons is not correlated (for example a readout problem that affects both electrons).

As a simple check, we do the complete analysis with no trigger requirement. Because a Z^0 event might pass several triggers, for the purposes of this check we assume that the `.OR.` of all triggers is fully efficient. We find that we gain 0 out of 103 C-C events, 4 out of 111 C-P events and 1 out of 39 C-F events, in agreement with our efficiency estimates from W electrons.

5.4 Estimation of Background

To estimate background from jet fluctuations, we loosen the isolation requirement and study the events around the Z^0 peak. We compare the isolation of the two legs and take the greater of the two values as an indicator for the event; this is referred to as *maximum isolation.* This is plotted versus mass in figure 5.14. We estimate the background by considering the events that neighbor our sample region of $75 < M < 105$ and $0 <$ max.iso. $< .1$. This accounts for both non-electrons (e.g. π^0 overlap with a stiff track) and real electrons that are non-isolated (e.g. semileptonic decay in b-quark jets).

We use three different methods to estimate the background. The first method estimate the amount of background in the Z region based on the number of the events in regions a plus c. The second method estimates the background from the number of events in region b, subtracting an estimate of the amount of Z^0 signal that has fluctuated into region b. The third method counts the events in regions d plus e and subtracts the number of Drell-Yan dielectrons we predict from Monte Carlo.

5.4.1 Method 1:

In the first method, we select events with both electrons passing all cuts but with isolation in the range $0.1 <$ Iso < 0.2. In figure 5.14 consider the events in the mass range 60 to 120 GeV. Above .1, this plot should contain mostly background, but could also have some Z events that fluctuate to poor isolation. The Z events should be mostly within the mass range 75 to 105 GeV. To avoid counting these in our estimate, we estimate the background from the side bands of 60-75 GeV and 105-115 GeV. There are a total of 9 events in this region, 8 in the low mass band and 1 in the high mass band. If we assume a background that falls linearly in mass and flat in maximum isolation, the background under the Z peak is 9 ± 3 events (figure 5.15). This estimate is pessimistic if the background falls faster than shown as a function of mass.

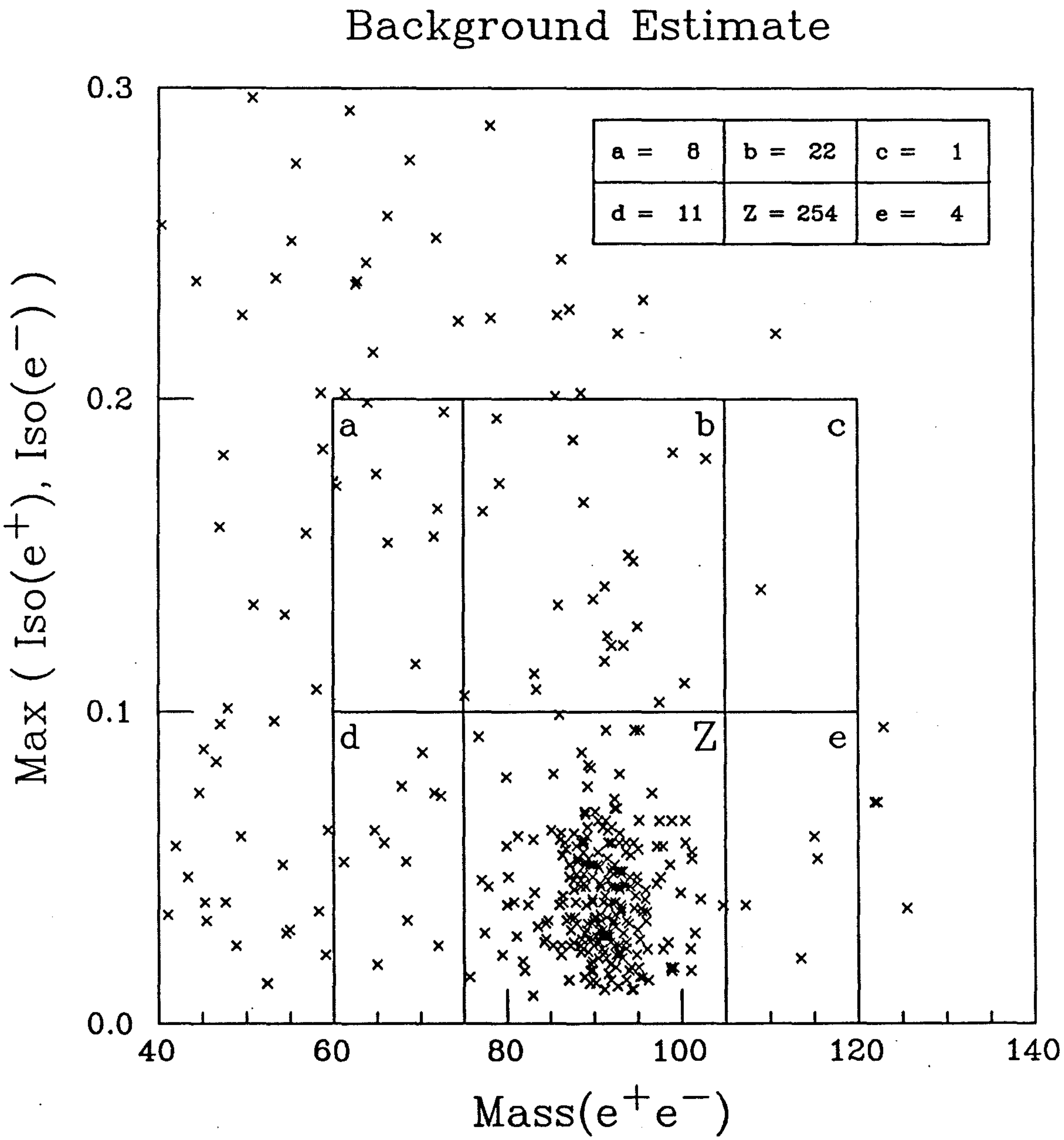

Figure 5.14: Estimation of background using space of maximum isolation versus mass. Note that the areas of $Z = b = a + c = d + e$.

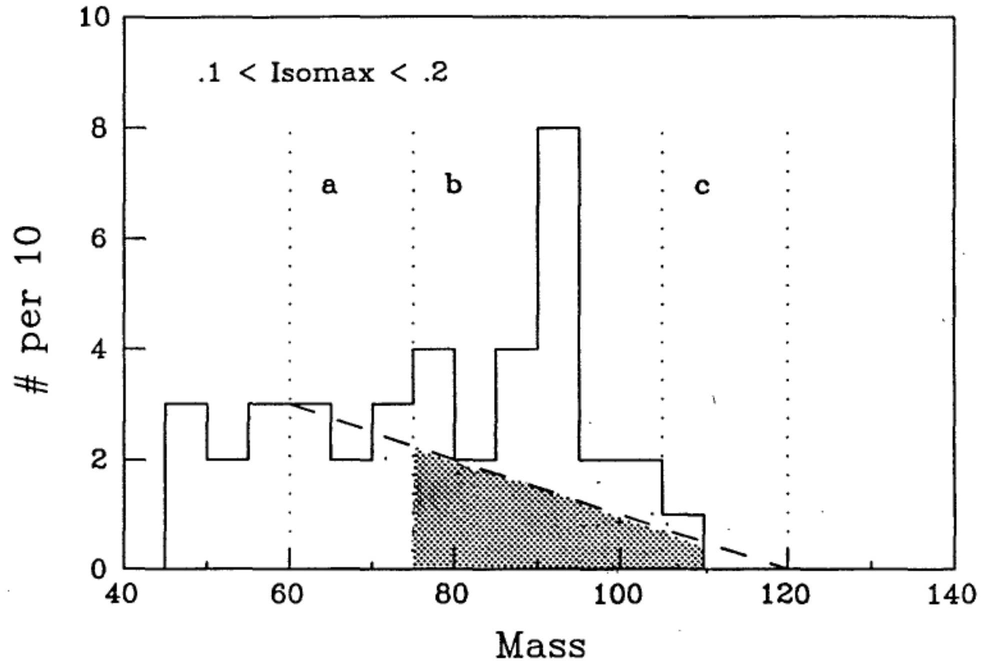

Figure 5.15: The background estimate of method 1. The gray area is a background of 9 events determined by the number of events in regions a and c.

5.4.2 Method 2:

In the second method, we consider the number of events in the mass region 75-105. We observe 22 events in this mass region with $.1 < \text{isolation} < .2$. In the previous section, we estimate that the isolation efficiency for an electron is .98. Because each event has two chances to have an electron fall out of the maximum isolation region $< .1$, the probability for an event to show a maximum isolation above .1 is $1 - .98^2 = .04$. Based on 254 events in the isolated Z^0 sample, there should be 10 ± 3 Z^0 events that fluctuated into failing the isolation cut. These fluctuated events are apparent as a peak at 90 GeV in figure 5.15. This leaves us with 12 background events in the region $75<\text{mass}<105$ with $.1<\text{max. iso.}<.2$ (figure 5.16). This agrees with the estimate from method 1. Assuming a flat spectrum as a function of maximum isolation, this predicts 12 ± 5 background events under the Z^0 peak.

However, the maximum isolation variable is not flat from .1 to 0. Because we are taking

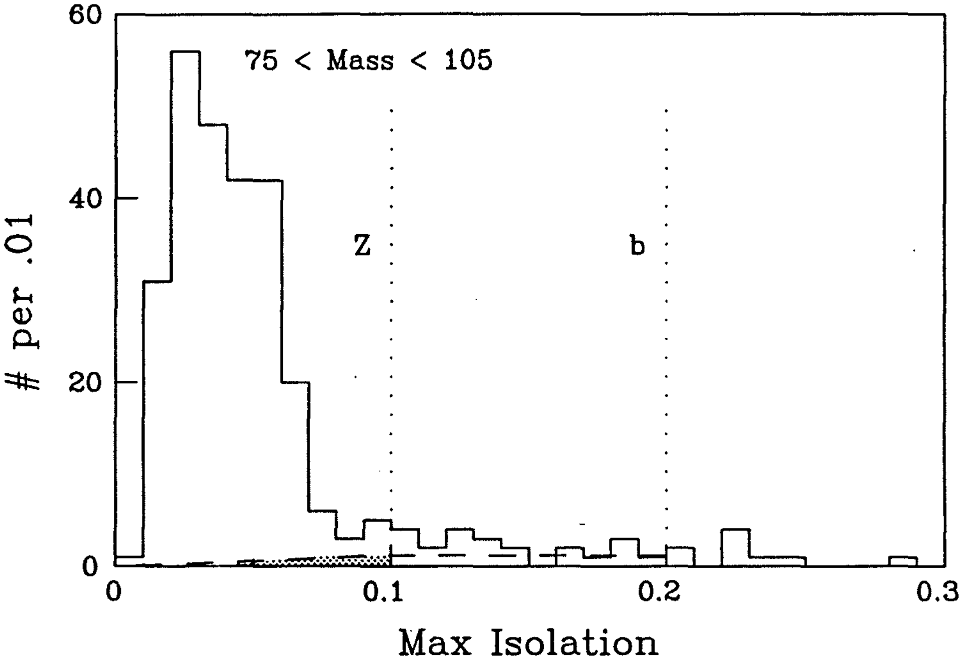

Figure 5.16: The background estimate of method 2. The gray area is a background of 6 events determined by the number of events in regions b, after subtracting an estimate of how many Z^0s have fluctuated to that region. We assume the number of background events in region Z is 1/2 the estimate in region b.

the maximum of two quantities that range from zero upward, the number of events must go to zero at maximum isolation = 0. Consider two uniform distributions from 0 to .3; if you select an independent number from each, the distribution of the maximum value will be a increase linearly from 0 to .3. Consider another case, where one of the distributions peaks at zero, similar to electron isolation (cf. figures 5.12a-c), the other distribution is flat. Drawing one value from each and taking the maximum results in a distribution that is flat at high values and then falls to zero. These exercises are illustrated in figure 5.17.

We have also considered the physical origins of the background events; these also indicate that maximum isolation falls to zero from .1 to 0. Figure 5.18 shows the distribution in maximum isolation for three different processes:

- Photon conversions are identified by matching tracks that intersect at a point not on the beamline [36].

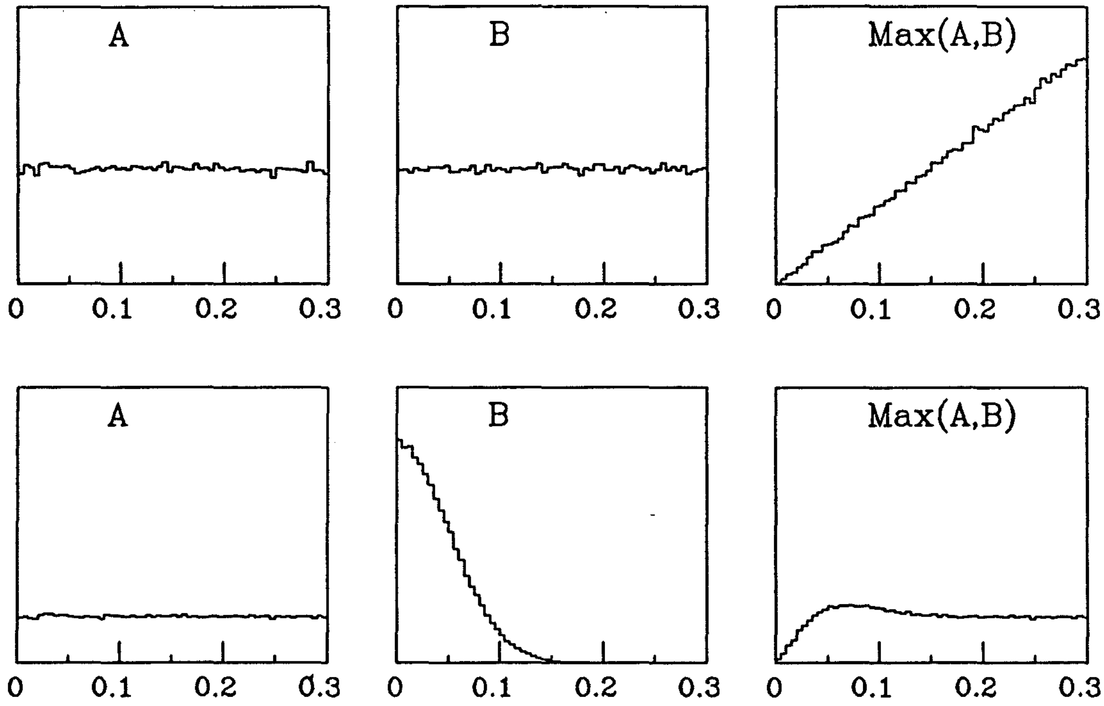

Figure 5.17: An illustration of the behavior of maximum isolation as determined from two separate distributions.

- Neutral EM clusters (π^0 candidates) are identified by requiring low hit occupancy in the VTPC (indicating the absence of a charged track) [35].
- Electron pairs from $b\bar{b}$ Monte Carlo [35].

These distributions also indicate that beneath the Z^0 peak, the background extrapolation in maximum isolation should tend to zero.

So instead of assuming a flat distribution in maximum isolation, we will assume the distribution is flat from .2 to .1 and falls linearly from .1 to 0. The background estimates of methods 1 and 2 are cut in half, to 5 ± 2 and 6 ± 4 background events respectively.

5.4.3 Method 3:

The third method corroborates a smaller background than 9-12 events. We take the number of events in side bands c and d, and subtract the predicted number of Drell-Yan plus Z^0 events. Using ISAJET with smearing and cutting on the electrons, we find that for 254

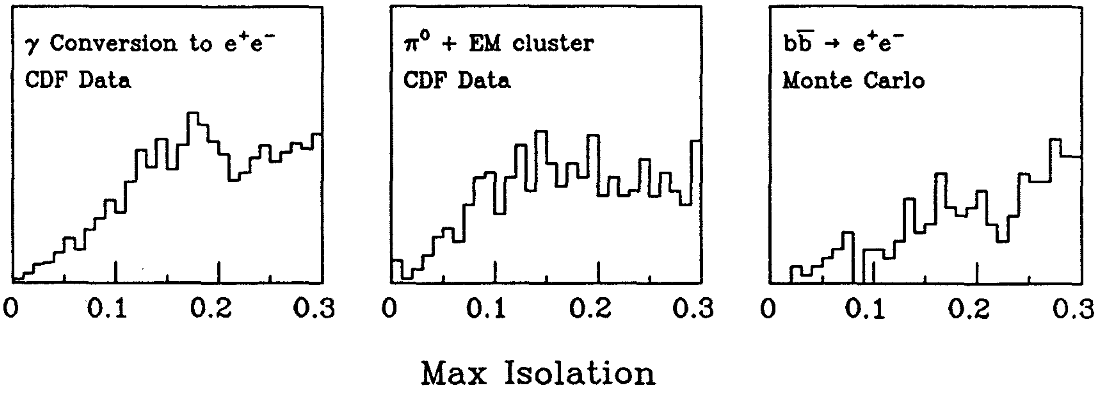

Figure 5.18: The behavior of maximum isolation for three physical processes.

events in the Z region, we expect 6.5 events between 60 and 75 GeV and 4.3 events between 105 and 120 GeV. We observe 11 and 4 events in those regions, respectively. The difference is a background estimate of 4 ± 3 events. As was mentioned for Method 2, this estimate is pessimistic if the background is falling more sharply as a function of mass.

Our three methods have estimated backgrounds of 5, 6 and 4 events under the Z^0 peak ($75 < \text{mass} < 105$ and $0.0 \leq \text{max. iso.} < 0.1$). We take as our final estimate 5 ± 3 events.

5.5 $Z^0 \to \tau^+\tau^-$

The background from Z^0 decaying to $\tau^+\tau^-$ where each τ then decays to $e\nu_e\nu_\tau$ is negligible. We generated this decay using the ISAJET Monte Carlo and applied the fiducial and kinematic ($E_t^e > 15$) requirements on each electron. The distribution of e^+e^- masses is shown in figure 5.19. We assume that $\sigma \cdot B(Z^0 \to \tau^+\tau^-)$ is the same as $\sigma \cdot B(Z^0 \to e^+e^-) \sim 200nb$. After taking into account a factor of $(.18)^2$ for the branching ratio for each τ to decay to $e\nu_e\nu_\tau$, we expect a total of 1 event to pass our cuts and only .02 events in the mass range from 75 to 105 GeV.

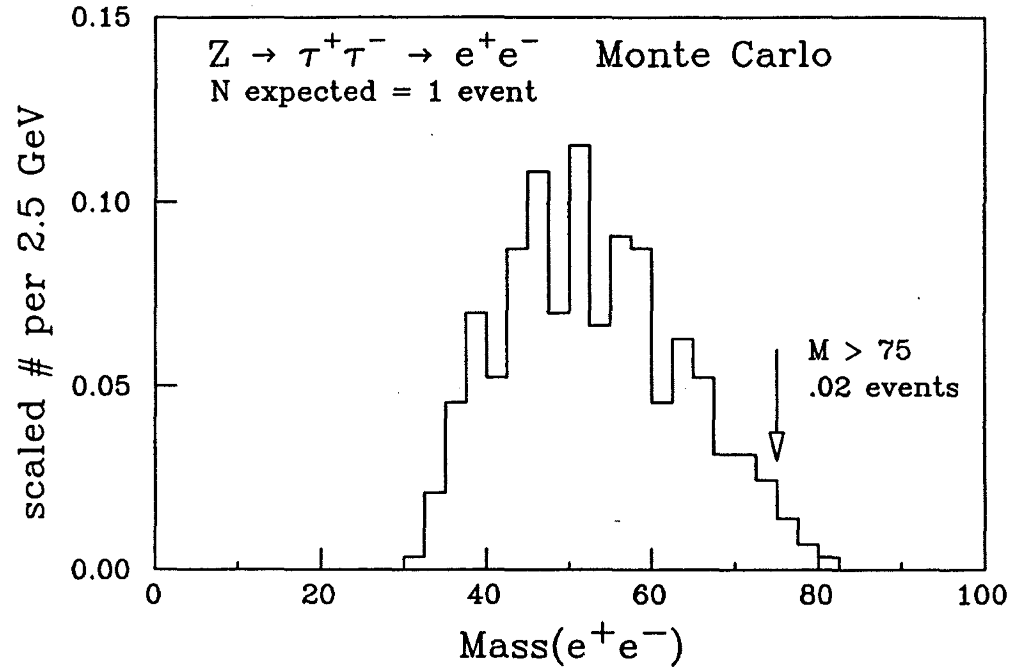

Figure 5.19: Mass distribution for $Z^0 \rightarrow \tau^+\tau^- \rightarrow e^+e^-$ + neutrinos. The number of events has been scaled to the expectation for our experiment.

5.6 Luminosity

The integrated luminosity for the data sample used in this analysis is 4.05 pb^{-1}, with an uncertainty of ±6.8%. The luminosity for each run is determined by the rate of coincidences in the BBC's (p. 22) using:

$$\mathcal{L} = \frac{R_{BBC}}{\sigma_{BBC}}. \tag{5.8}$$

During the 1988-1989 run the instantaneous luminosity varied from 2×10^{29} to $2 \times 10^{30}/\mathrm{cm}^2/\mathrm{sec}$. The BBC rate was corrected to account for multiple interactions (typically 8% at $\mathcal{L}_{inst} = 10^{30}$).

The scale of the integrated luminosity for our data sample is determined by our estimate of the BBC cross section, σ_{BBC}, at $\sqrt{s} = 1800$ GeV [38]. We estimate $\sigma_{BBC}(1800)$ by scaling a separate estimate of σ_{BBC} at $\sqrt{s} = 546$ GeV using:

$$\frac{\sigma_{BBC}(1800)}{\sigma_{BBC}(546)} = \frac{\frac{R_{BBC}(1800)}{\mathcal{L}_{acc}(1800)}}{\frac{R_{BBC}(546)}{\mathcal{L}_{acc}(546)}}. \tag{5.9}$$

Here we are using accelerator estimates of the luminosity, $\mathcal{L}_{acc}$, that have an overall uncertainty of 11%, but a relative uncertainty of only 4.3%.

The value of $\sigma_{BBC}(546)$ is the weighted average of two independent estimates. The first estimate relies on a measurement of $\sigma_{tot}^{\bar{p}p}$ at 546 GeV by the UA4 collaboration [39]. The UA4 measurement is derived from a double arm trigger rate with acceptance similar to the CDF BBC's. UA4 uses the standard method [40] of simultaneously measuring the total interaction rate ($R_{elastic} + R_{inelastic}$), the differential elastic scattering rate (dR_{elast}/dt) extrapolated to $t = 0$ and the ratio of the real to imaginary part of the forward elastic scattering amplitude (ρ):

$$\sigma_{tot} = \frac{1}{(1+\rho^2)} \frac{16\pi(hc)^2}{R_{elastic} + R_{inelastic}} \frac{dR_{elastic}}{dt}\Big|_{t=0}. \tag{5.10}$$

UA4 obtains a value for σ_{tot} of 59.5 ± 1.8 mb. We derive an effective trigger counter cross section at UA4 of $\sigma_{trig}^{\mathrm{UA4}} = 38.9 \pm 1.8$ mb. We use a minimum bias Monte Carlo to calculate a correction factor to account for the difference in acceptance (A_η) between the UA4 trigger counters and the CDF BBC's. Combining that with our measurement of the CDF BBC inefficiency, we obtain:

$$\begin{aligned} \sigma_{BBC}(546) &= \left(\frac{A_\eta^{BBC}}{A_\eta^{\mathrm{UA4}}}\right)(\epsilon^{BBC})\sigma_{trig}^{\mathrm{UA4}} \qquad (5.11)\\ &= (.975 \pm .024)(.978 \pm .022)(38.9 \pm 1.8\mathrm{mb}) \\ &= 37.1 \pm 2.1 \text{ mb.} \end{aligned}$$

The second estimate of $\sigma_{BBC}(546)$ is derived from measurements of colliding beam parameters provided by the Fermilab Accelerator Division during special low energy runs at $\sqrt{s} = 546$ GeV GeV. At regular intervals during a run, wires are passed through the beam to measure the transverse profile of the bunches, σ_x and σ_y. A resistive wall current monitor measures the longitudinal profiles, σ_z, and the intensity of the bunches, N_p and $N_{\bar{p}}$. The momentum dispersion, dp/p, is derived from the bunch profiles and the measured RF voltage. During each run an online monitoring program records these parameters and calculates the run luminosity based on the following formula for the luminosity of two bunches crossing:

$$\mathcal{L} = N_p N_{\bar{p}} \int \frac{1}{\sqrt{2\pi}\,\sigma_z} \frac{e^{-\frac{z^2}{2\sigma_z^2}}}{4\pi\,\sigma_x(z, \frac{dp}{p})\,\sigma_y(z, \frac{dp}{p})} dz. \tag{5.12}$$

Using the accelerator estimate of the luminosity and the measured rate in the BBC's during 546 GeV running, we estimate $\sigma_{BBC}(546) = 32.8 \pm 3.6$ mb.

We again use the accelerator estimates of the luminosity, in conjunction with the measured BBC rate to scale $\sigma_{BBC}(546)$ to 1800 GeV. Here many of the uncertainties in $\mathcal{L}_{acc}$ cancel out in the ratio used in equation 5.9. We calculate a scaling factor of $1.303 \pm .056$ to adjust $\sigma_{BBC}(546)$ to $\sigma_{BBC}(1800)$. The weighted average of $\sigma_{BBC}(546)$ from the two independent estimates is 36.0 ± 1.8 mb. Combining these numbers we obtain an estimated BBC cross section at $\sqrt{s} = 1800$ GeV of 46.8 ± 3.2 mb.

5.7 Result

Table 5.4 lists the values that are used to calculate the cross section and its uncertainty. The formula used is:

$$\sigma \cdot B(Z^0 \to e^+e^-) = \frac{N_Z \cdot f_{DY} - N_{bg}}{a_{ee\gamma}\epsilon_{\mathrm{zv}}(a_{cc}\epsilon_{c1}(2\epsilon_{c2} - \epsilon_{c1})i_c^2 t_{cc} + a_{cp}\epsilon_{c1}\epsilon_p i_c i_p t_{cp} + a_{cf}\epsilon_{c1}\epsilon_f i_c i_f t_{cf}) \cdot \mathcal{L}}. \tag{5.13}$$

The term $\epsilon_{c1}(2\epsilon_{c2} - \epsilon_{c1})$ takes into account the combinatorics for C-C events. The following table lists the probabilities for a good C-C event in terms of the efficiency for each electron; the total probability is the term in question:

case	electron 1	electron 2
both electrons pass tight cuts	ϵ_{c1}	ϵ_{c1}
one tight, other loose but not tight	ϵ_{c1}	$\epsilon_{c2} - \epsilon_{c1}$
one loose but not tight, other tight	$\epsilon_{c2} - \epsilon_{c1}$	ϵ_{c1}
total:	$\epsilon_{c1}(2\epsilon_{c2} - \epsilon c1)$	

The term $\epsilon_{c2} - \epsilon_{c1}$ is appropriate because the cuts for the loose electron are a subset of the cuts for the tight electron.

The result is:

$$\sigma \cdot B(Z^0 \to e^+e^-) = 218 \pm 14(\text{stat.}) \pm 7(\text{sys.}) \pm 15(\text{lum.})\ \text{pb}.$$

The statistical uncertainty is from the number of Z events. The systematic uncertainty is calculated by propagating each of the uncertainties listed in table 5.4 in quadrature. We are assuming the systematic uncertainties are uncorrelated, with the exception of the uncertainties in acceptance due to choice of structure function. Because the variables a_{cc}, a_{cp} and a_{cf} are correlated, we take the total contribution to the systematic error from acceptance as 3 pb; this is the maximum change in the final result found by trying an assortment of structure functions (see section 5.2.3). The uncertainty in luminosity is 6.8%.

Variable	Value ± Uncertainty		Description	page no.
N_Z	254.0	15.94	Number of $Z0$s	37
a_{cc}	0.139	0.002	C-C Acceptance	44
a_{cp}	0.166	0.002	C-P Acceptance	44
a_{cf}	0.058	0.002	C-F Acceptance	44
$a_{ee\gamma}$	0.992	0.005	$ee\gamma$ Acceptance	48
ϵ_{c1}	0.873	0.023	C Tight Selection Efficiency	52
ϵ_{c2}	0.941	0.016	C Loose Selection Efficiency	52
ϵ_p	0.941	0.022	P Selection Efficiency	49
ϵ_f	1.000	0.025	F Selection Efficiency	49
i_c	0.985	0.010	C Isolation Efficiency	54
i_p	0.976	0.010	P Isolation Efficiency	54
i_f	0.977	0.020	F Isolation Efficiency	54
t_{cc}	0.999	0.001	C-C Trigger efficiency	58
$t_{cp} = t_{cf}$	0.969	0.001	C-P and C-F Trigger efficiency	58
ϵ_{zv}	0.959	0.005	z-vertex efficiency	57
N_{bg}	5.000	3.000	Background Estimate	64
f_{DY}	0.987	0.005	D-Y Correction Factor	10
$\mathcal{L}$	4.052	0.276	Luminosity (pb^{-1})	65

Table 5.4: Numbers used in the calculation of the total Z^0 cross section

The final result is plotted in figure 5.20 with the theoretical curves of section 2.3. The order α_s calculation of reference [19] has an estimated theoretical uncertainty of 10%. The CERN measurements at lower $\sqrt{s}$ are also shown [6] [41]. The increase in cross section from our higher center-of-mass energy is apparent. The result is significantly greater than the Born level prediction, indicating the important higher order contributions to the cross section. The result is in agreement with the higher order calculations, but is not accurate enough to discriminate between the order α_s and order α_s^2 calculations.

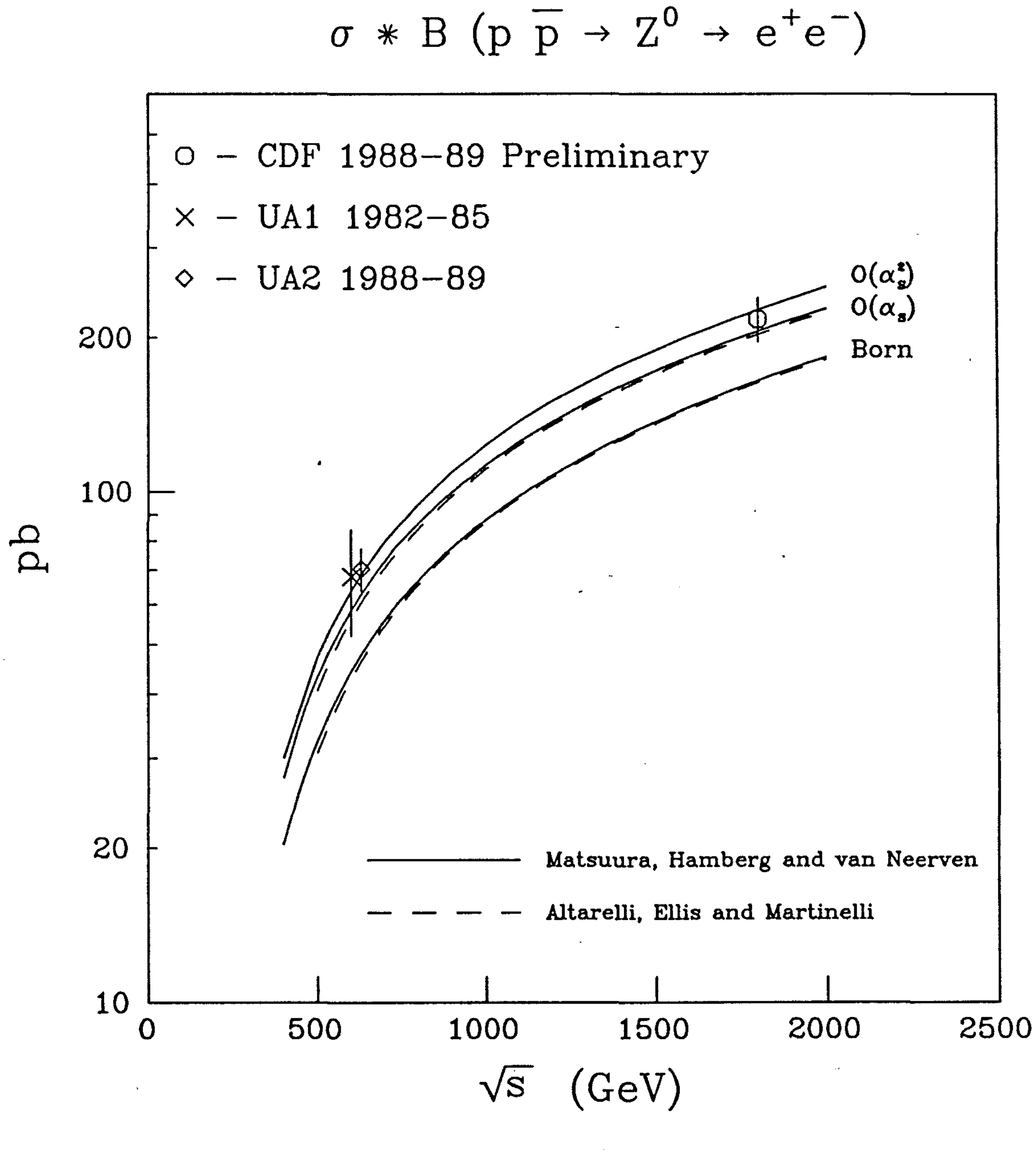

Figure 5.20: Our measurement of $\sigma \cdot \mathrm{B}(Z^0 \rightarrow e^+e^-)$ compared with theory and other experiments.

Bibliography

[1] S.L. Glashow, *Nucl. Phys.* **22** (1961) 579; A. Salam in **Elementary Particle Theory**, ed. N. Svartholm (Almqvist and Wiksell, Stockholm, 1968); S. Weinberg, *Phys. Rev. Lett.* **19** (1967) 1264

[2] G. Arnison et al. (UA1 Collaboration), *Phys. Lett.* **B122** (1983) 103

[3] M. Banner et al. (UA2 Collaboration), *Phys. Lett.* **B122** (1983) 476

[4] G. Arnison et al. (UA1 Collaboration), *Phys. Lett.* **B126** (1983) 398

[5] M. Banner et al. (UA2 Collaboration), *Phys. Lett.* **B129** (1983) 130

[6] C. Albajar et al. (UA1 Collaboration), *Zeitschrift fur Physics* **C44** (1989) 15

[7] R. Ansari et al. (UA2 Collaboration), *Phys. Lett.* **B194** (1987) 15

[8] C.N. Yang and R. Mills. *Phys. Rev.* **96** (1954), 191

[9] P. Higgs, *Phys. Rev.* **145** (1966) 1156

[10] E. Fermi, Nuovo Cimento **11** (1934) 1
E. Fermi, *Zeitschrift fur Physics* **88** (1934) 161

[11] U. Amaldi et al., *Phys. Rev.* **D36**, (1987) 1385

[12] F. Abe et al., to be submitted to *Phys. Rev. Lett.* and *Phys. Rev.* **D**
W. Trischuk, Ph.D. Thesis, Harvard University, May 1990

[13] F. Abe et al., to be submitted to *Phys. Rev. Lett.*

P. Hurst, Ph.D. Thesis, University of Illinois, July 1990

[14] S. Drell and T.M. Yan, *Phys. Rev.* **25** (1970) 316; *Ann. of Phys.* **66** (1971) 578

[15] G. Altarelli and G. Parisi, *Nucl. Phys.* **B126** (1977) 298

[16] G. Altarelli, M. Diemoz, G. Martinelli and P. Nason, *Nucl. Phys.* **B308** (1988) 724

[17] Diemoz, Ferroni, Longo and Martinelli, *Zeitschrift fur Physics* **C39**, (1988) 21

[18] G. Altarelli, R.K. Ellis and G. Martinelli, *Zeitschrift fur Physics* C27 (1985) 617

G. Altarelli, R.K. Ellis, M. Greco and G. Martinelli, *Nucl. Phys.* B246 (1984) 12

[19] R.K. Ellis, *Proceedings of the 8th Topical Workshop on Proton Antiproton Collider Physics*, Castiglione della Pescaia, 1988.

[20] T. Matsuura, S.C. van der Marck and W.L. van Neerven, *Nucl. Phys.* B319 (1989) 570

T. Matsuura, R. Hamberg and W.L. van Neerven, DESY preprint 90-031

[21] L. Rolandi, CERN-EP/90-64, presented at XXVth Rencontres de Moriond, Les Arcs, March 1990

[22] (CDF Collaboration), The Collider Detector at Fermilab: A compilation of articles reprinted from Nuclear Instruments and Methods in Physics Research-A, North-Holland Physics Publishing, 1988

[23] F. Abe et al. (CDF Collaboration), *Phys. Rev. Lett.* **63** (1989) 720

[24] G.S. Abrams et al. (Mark-II Collaboration), *Phys. Rev. Lett.* **63** (1989) 724 G.S. Abrams et al. (Mark-II Collaboration), *Phys. Rev. Lett.* **63** (1989) 2173

[25] Particle Data Group, to be published

B. Adeva et al., (L3 Collaboration), *Phys. Lett.* **B231** (1989) 509

D. DeCamp et al., (ALEPH Collaboration), *Phys. Lett.* **B231** (1989) 519

M. Akrawy et al., (OPAL Collaboration), *Phys. Lett.* **B231** (1989) 530

P. Aarnio et al., (DELPHI Collaboration), *Phys. Lett.* **B231** (1989) 539

[26] E. Kearns, CDF Note 1077

[27] J. Ng, CDF Note 968

[28] F.E. Paige and S.D. Protopopescu, BNL Theoretical Paper **37066** (1985)

[29] Eichten, Hinchliffe, Lane and Quigg, *Reviews of Modern Physics* **58**, (1986) 1065

[30] Duke and Owens, *Phys. Rev.* **D30**, (1984) 49

[31] Martin, Roberts and Stirling, *Phys. Rev.* **D37**, (1988) 1161

[32] P.N. Harriman, A.D. Martin, R.G. Roberts and W.S. Stirling, preprint DTP/90/04 or RAL/90/007, April 1990

[33] M. Mangano and R.G. Wagner, CDF Note 1009

[34] F.A. Berends, R. Kleiss, J.P. Revol and J.P. Vialle, *Zeitschrift fur Physics* **C27** (1985) 155

F.A. Berends and R. Kleiss, *Zeitschrift fur Physics* **C27** (1985) 365

[35] M. Gold, A. Yagil, A. Clark, CDF Note 1094

[36] M. Gold, CDF Note 913

[37] J. Proudfoot, CDF Note 1008

[38] C. Grosso-Pilcher and S. White, CDF Note 1202

[39] M. Bozzo et al., (UA4 Collaboration), *Phys. Lett.* **B147** (1984) 392

D. Bernard et al., (UA4 Collaboration), *Phys. Lett.* **B198** (1987) 583

[40] U. Amaldi, in *Laws of Hadronic Matter* A. Zichichi ed. (1975) p. 673

[41] J. Alitti, et al., CERN-EP/90-20 (1990)